Acta Pharmaceutica Sinica B 2026;16(7):4367−4388

Chinese Pharmaceutical Association
Institute of Materia Medica, Chinese Academy of Medical Sciences

Acta Pharmaceutica Sinica B

www.elsevier.com/locate/apsb
www.sciencedirect.com

ORIGINAL ARTICLE

PYGL-driven glycogenolysis impairs microglial autophagic flux *via* SNAP29 *O*-GlcNAcylation in Alzheimer's disease

Yi Ding[a,†], Shi-Yao Li[a,†], Wen-Feng Zhang[a,†], Mao-Mao Chu[a], Xue-Jie Wang[a], Yu-Ge Zhang[a], Hui-Wen Zhang[a], Yu-Tong Zhang[a], Lu Xu[a], Xue Liu[a], Tsuyoshi Morita[b], Otto Baba[b], Zi-Jian Ren[c,d], Yong-Jie Zhang[c,d,*], Zhi-Yuan Zhang[a,e,f,*], Lei Li[a,*]

[a]*School of Basic Medical Sciences, Nanjing Medical University, Nanjing 211166, China*
[b]*Oral and Maxillofacial Anatomy, Tokushima University Graduate School, Tokushima 770-8504, Japan*
[c]*Department of Human Anatomy, Nanjing Medical University, Nanjing 211166, China*
[d]*Human Brain Tissue Resource Center, Nanjing Medical University, Nanjing 211166, China*
[e]*Jiangsu Key Laboratory of Neurodegeneration, Nanjing Medical University, Nanjing 211166, China*
[f]*Department of Neurology, Sir Run Run Hospital, Nanjing Medical University, Nanjing 211112, China*

Received 2 September 2025; received in revised form 20 January 2026; accepted 17 February 2026

KEY WORDS

Glycogen metabolism;
Glycogenolysis;
PYGL;
O-GlcNAcylation;
SNARE complex;
SNAP29;
Autophagosome−lysosome fusion;
Autophagy

Abstract Aberrant metabolic alterations underlie microglial dysfunction, which plays an important role during neurodegenerative progression. However, the role of aberrant glycogen metabolism remains elusive. Here, we identified glycogen accumulation and upregulated glycogenolytic enzymes in brain microglia from patients with Alzheimer's disease (AD) and transgenic animal models. Particularly, the principal microglial glycogenolytic enzyme PYGL exhibited the most notable spatiotemporal upregulation during disease progression. Specific knockdown of microglial PYGL ameliorated neuropathological changes and cognitive deficits in AD mice. Bioinformatics analysis and experimental validation confirmed that enhancing microglial autophagic flux-dependent Aβ clearance was the underlying mechanism. Furthermore, among all possible glycogenolytic pathways, PYGL downregulation primarily reduced hexosamine biosynthesis pathway activity, diminished UDP-GlcNAc and *O*-GlcNAcylation of the autophagy key protein SNAP29, and thereby facilitated formation of the SNARE complex,

*Corresponding authors.
E-mail addresses: NJMULL@njmu.edu.cn (Lei Li), zzy@njmu.edu.cn (Zhi-Yuan Zhang), zhangyongjie@njmu.edu.cn (Yong-Jie Zhang).
[†]These authors made equal contributions to this work.
Peer review under the responsibility of Chinese Pharmaceutical Association and Institute of Materia Medica, Chinese Academy of Medical Sciences.

https://doi.org/10.1016/j.apsb.2026.04.017

which is essential for autophagosome−lysosome fusion. These findings reveal a glycogenolysis-driven post-translational pathway regulating microglial autophagy, establishing PYGL as a therapeutic target for AD.

1. Introduction

Alzheimer's disease (AD) is a progressive, fatal neurodegenerative disorder characterized by excessive accumulation of β-amyloid (Aβ) plaques, neurofibrillary tangles of hyperphosphorylated tau protein, and substantial neuronal loss[1,2]. Metabolic dysregulation, including glucose utilization and altered lipid metabolism, is increasingly recognized as an early hallmark of AD progression[3]. Notably, brain hypometabolism detected by FDG-PET precedes cognitive decline and correlates with amyloid burden[4].

Recent genome-wide association studies have revealed that microglial dysfunction is a key pathogenic driver[5,6]. Microglial plasticity, which denotes their ability to adapt functionally and phenotypically to environmental stimuli, is tightly regulated by metabolic flexibility[7-10]. In particular, the well-identified AD risk genes *TREM2* and *APOE* have been shown to regulate multiple metabolic pathways such as glucose, lipid, and amino acid metabolism, influencing microglial energy balance, immune responses, and phagocytic activity, thereby revealing their complex links to AD pathology[11-14]. Moreover, growing evidence suggests that aberrant metabolic alterations underlie microglial dysfunction during AD progression[15,16]. For instance, increased expression of PKM2 promotes lactate-mediated histone lactylation and thereby drives proinflammatory microglial activation in AD[15]. However, the metabolic profile of microglia during AD progression, and how their aberrant metabolic changes contribute to AD pathological progression, remain unclear.

Glycogen is an important glucose storage molecule essential for maintaining physiological function and energy balance[17]. Glycogen metabolism involves processes such as glycogen synthesis and glycogenolysis, which are primarily regulated directly by glycogen synthases (GYS) and glycogen phosphorylases (PYG), respectively. Glycogen-derived metabolites serve not only as energy sources but as key regulators of immune signaling, influencing redox balance and transcriptional activation. For instance, during macrophage activation, glycogenolysis fuels the pentose phosphate pathway (PPP) to generate NADPH and glutathione for redox control, while providing UDP-glucose (UDPG) for transcriptional regulation of inflammatory genes[18]. Notably, emerging studies have reported an important role for glycogen catabolism in aging and cognitive disorders[19,20]. For instance, prostaglandin E2 signaling has been shown to promote glycogen synthesis in peripheral monocytes, while its inhibition suppressed inflammatory responses and restored spatial memory in aged mice[19]. Moreover, prolonged inhibition of glycogen phosphorolysis could improve age-related memory deficits[20], although the underlying mechanism has not been investigated. While glycogen metabolism has been extensively characterized in peripheral immune cells[18,21,22], its role in central nervous system (CNS) immunity remains largely unexplored. As resident immune cells in the CNS, microglia exhibit glycogen accumulation during AD pathogenesis, with glycogen granules potentially serving as a distinctive feature that distinguishes dark microglia from other microglial phenotypes. In particular, glycogen-enriched dark microglia predominantly localize adjacent to Aβ plaques and dystrophic neurites in the hippocampus of AD mice[22], suggesting a potential link between glycogen metabolism and disease-associated microglial phenotypes. However, the regulatory mechanisms and functional outcomes of microglial glycogen metabolism remain undefined.

In this study, we identified aberrant changes in glycogen metabolism alterations of microglia in patients with AD and transgenic model mice. Moreover, we demonstrated that PYGL-mediated glycogenolysis has a central function in controlling microglial autophagy through the hexosamine biosynthesis pathway (HBP)-mediated *O*-GlcNAcylation pathway during AD progression. Collectively, we reveal a novel immunometabolic mechanism through which glycogen catabolism regulates autophagic function, proposing microglial PYGL as a potential therapeutic target for AD.

2. Materials and methods

2.1. Antibodies and reagents

All reagents, commercial kits, and antibodies were listed in Supporting Information Table S1.

2.2. Animals

C57BL/6 wild-type (WT) mice and Sprague Dawley neonatal rats were obtained from the Nanjing Medical University Medical Experimental Animal Center (Nanjing, China). APP/PS1-21 transgenic mice were provided by Prof. M. Jucker (University of Tuebingen, Germany). The 5 × FAD transgenic mice were acquired from Aniphe Biolaboratory Inc. (Nanjing, China). All animals were housed in a specific pathogen-free barrier facility under controlled conditions (20−26 °C, 12-h light/dark cycle, 30%−70% humidity) with *ad libitum* access to food and water. Although AD affects both sexes, to eliminate the confounding effects of estrogen, only male mice were used in this study. Primary cell culture experiments were conducted using Sprague Dawley neonatal rats at postnatal Days 1−2, maintained under specific pathogen-free conditions. All animal procedures were approved by the Animal Care and Use Committee of Nanjing Medical University and conducted in accordance with the Guide for the Care and Use of Laboratory Animals (Approval No. 1904008).

2.3. Human brain tissues

Frozen hippocampal tissues from three patients with AD and three controls were obtained from the Nanjing Medical University Brain Bank (Approval No. 2022-816), following the Declaration of Helsinki. The patient information is summarized in Supporting

Information Table S2. All participants were fully aware of the goal and possible risk of this study and provided written informed consent. This study was performed in accordance with the Declaration of Helsinki.

2.4. Injection of adeno-associated virus (AAV)

The mouse was anesthetized *via* inhalation of isoflurane and then placed in a stereotaxic frame, with the head securely fixed to ensure a horizontal position. After disinfecting the scalp with povidone-iodine and removing the hair, a midline scalp incision was made using sterilized scissors to expose the skull. The skull surface was cleaned with medical-grade hydrogen peroxide to clearly identify the Bregma landmark. Using a microsyringe, 0.5 μL of virus was bilaterally injected into two anterior−posterior sites of the hippocampus. The coordinates for the anterior hippocampal site were as follows: Bregma, −1.55 mm; lateral, ±1 mm; and depth, 2 mm. The posterior hippocampal site coordinates were: Bregma, −2.7 mm; lateral, ±2 mm; and depth, 2 mm. Following the injection, the needle was left in place for 10 min before being slowly withdrawn. The scalp incision was then sutured and disinfected again, and the mice were monitored continuously until full recovery. The AAV viruses used in this study were all constructed and provided by Brain Case Biotechnology Co., Ltd., (Shenzhen, China). The vector serotype was AAV11, with a titer of 1×10^{13} vg/mL. The shRNA sequence for AAV-PYGL-cKD was 5′-TGGAAGAGTTAGAAGAAAT-3′. The complete construct for AAV-NC was: pAAV-mIBA1-EGFP-5′miR-30a-shRNA (Scramble)-3′miR-30a-WPRE-4 × miR9T, and the complete construct for AAV-PYGL-cKD was: pAAV-mIBA1-EGFP-5′miR-30a-shRNA(mPygl)-3′miR-30a-WPRE-4 × miR9T.

2.5. Behavioral tests

2.5.1. Morris water maze

The Morris water maze test was performed in a circular pool divided into four quadrants. Mice were randomly placed at one of the four starting positions, and the time taken to locate the submerged platform (escape latency) was recorded. Each animal underwent four training trials per day with 15 min intervals between trials for 5 consecutive days. During the training phase, the escape latency and the number of platform crossings were measured and analyzed. One day after the last training session, probe trials were conducted to assess spatial memory. During the probe test, the swimming speed, the number of platform crossings, and the time spent in the target quadrant were recorded and analyzed.

2.5.2. Novel object recognition test (NORT)

This test leverages the innate curiosity of mice and their tendency to explore novel objects. On the first day (habituation phase), each mouse was placed in an open-field box for 5 min. During the familiarization phase, two identical cylindrical objects were placed in the box, and each mouse was allowed to explore for 5 min to become familiar with the objects. In the test phase, one linder was replaced with a square object, and the mice were reintroduced to the box for exploration. The frequency and duration of interaction with the novel object were recorded. After each session, the box was cleaned with 75% ethanol to remove olfactory cues. Recognition index was calculated according to Eqn 1:

$$\text{Recognition index (\%)} = \text{Number of novel object explorations} / (\text{Number of novel} + \text{Familiar object explorations}) \times 100 \quad (1)$$

A higher recognition index indicates better cognitive function.

2.5.3. Fear conditioning test (FCT)

One day before training, the mice were placed in the conditioning chamber for a 5 min habituation period. During the training phase, the mice were placed in the chamber for 180 s before receiving a 30 s auditory stimulus (90 dB, 5000 Hz), followed by a 2 s foot shock (0.8 mA). After a 30 s interval, the auditory stimulus and foot shock were repeated. Following the final foot shock, the mice remained in the chamber for an additional 60 s before being returned to their home cages. The chamber was cleaned with 75% ethanol after each session to eliminate residual odors. During the test phase, mice were exposed only to an auditory stimulus (30 s duration, 100 s interstimulus intervals). The percentage of freezing time was recorded and analyzed to assess fear memory.

2.6. Immunofluorescence

The mouse was anesthetized by intraperitoneal injection of sodium pentobarbital and perfused with PBS, followed by fixation with 4% paraformaldehyde. Fixed brains were dehydrated in 30% sucrose solution at 4 °C for 3−4 days, with daily solution changes until the tissues sank. The brains were embedded in OCT compound and snap-frozen at −20 °C for 1−2 days. Fully frozen tissues were equilibrated in a cryostat for 2 h before sectioning at 15 μm. The sections were stored in fixative at −20 °C. For staining, the sections were placed on slides, permeabilized with 0.2% Triton X-100 for 10 min at room temperature, and blocked with 1% bovine serum albumin (BSA) for 1 h. Primary antibodies were added and incubated overnight at 4 °C, followed by three washes with PBST. The secondary antibodies were added and incubated for 1 h at room temperature in the dark. Finally, the slides were mounted with DAPI and imaged. The following antibodies were used for immunofluorescence: PYGL (rabbit, 1:1000), ESG1A9 (mouse, 1:50), Iba1 (goat, 1:200), and Aβ (mouse, 1:200). Fluorescent secondary antibodies (1:500) for 488/555/647 were purchased from Abcam.

In immunofluorescence detection, the acquisition of images from each channel was performed using a laser scanning confocal microscope (LSM900, ZEISS, Oberkochen, Germany) with a resolution setting of 1024 × 1024 pixels. Fluorescence signals were identified based on a threshold exceeding 30% of the maximum fluorescence intensity of the image, and subsequent statistical analysis was conducted using specific fluorescent antibodies corresponding to each target and their respective imaging channels. All experimental images included clear scale bars and were captured randomly within the corresponding tissue regions or cell culture systems.

For assessing glycogen content in microglia, the same laser scanning confocal microscope with a 63× oil immersion objective was used to randomly select and image Iba1-positive microglial cells. Glycogen fluorescence staining employed the ESG1A9 antibody[23,24] developed by Prof. Otto Baba's laboratory, whose fluorescence signal also appears green. The imaging resolution was 1024 px × 1024 px, and the fluorescence threshold was similarly set at 30% of the maximum fluorescence intensity. Quantification of glycogen particles was performed using the Analyze Particles function in ImageJ software. For each randomly

captured microglial cell showing both DAPI and Iba1-positive signals, green fluorescent spots with intensities above the 30% threshold were identified and counted.

In the 3D reconstruction of glycogen, images were acquired using a 63× oil immersion objective on the laser scanning confocal microscope with the following settings: resolution 1024 px × 1024 px, Scan speed: 6. The z-stack acquisition parameters were configured as follows: slices: 15, Interval: 1 μm, Optimal: 0.5 μm. After image acquisition, professional 3D analysis software Imaris (version 9.0.1) was used for 3D reconstruction, with surface detail in smooth set to 0.4 μm and absolute intensity in thresholding set to 20. In the 3D reconstruction, images were acquired using a 63 × oil immersion objective on the laser scanning confocal microscope with the following settings: resolution 1024 px × 1024 px, Scan speed: 5. The z-stack acquisition parameters were configured as follows: slices: 10, Interval: 1 μm, Optimal: 0.5 μm. After image acquisition, professional 3D analysis software Imaris (version 9.0.1) was used for 3D reconstruction, with surface detail in smooth set to 0.3 μm and absolute intensity in thresholding set to 30. This quantification criterion is consistent with that used in previous literature for 3D reconstruction of dual immunofluorescence staining of Aβ (green) and Iba1 (red) in the hippocampal region of AD mice[16]. Therefore, in this study, we also performed 3D reconstruction based on dual immunofluorescence staining of Aβ (green) and Iba1 (red) in the hippocampal region of AD mice. Quantitative analysis of all fluorescence images was conducted using the Analyze Particles function in ImageJ software. For each randomly captured field of view, the system extracted pixel regions where the fluorescence intensity exceeded 30% of the maximum intensity in the red channel (Iba1-labeled) and green channel (Aβ), respectively, and calculated their areas. Regions where red and green signals overlapped were identified as Aβ and Iba1 co-localization areas. Finally, the degree of co-localization was quantified using the following formula: area of red-green overlap/total area of green signal.

2.7. *RNA-fluorescence in situ hybridization (RNA-FISH)*

RNA-FISH was performed following the manufacturer's protocol (BersinBio, Guangzhou, China). Briefly, frozen tissue sections were retrieved from −80 °C and rapidly transferred to a slide warmer for 30 min at 56 °C. The sections were fixed in 90% ethanol at 4 °C for 20 min and then air-dried at room temperature. After permeabilization for 10 min and three washes, the sections were post-fixed in 1% paraformaldehyde for 10 min, followed by additional washes. The sections were dehydrated in an ethanol gradient (70%, 80%, 90%, and 100%, 5 min each) and air-dried. A mixture of probe and hybridization buffer was applied to the sections, denatured at 73 °C for 5 min, and hybridized overnight at 42 °C. The sections were washed, counterstained with DAPI, mounted, and visualized using fluorescence microscopy. For image acquisition, a 63× oil immersion objective on a laser scanning confocal microscope (LSM900, ZEISS) was used, with an image resolution set at 1024 px × 1024 px and a scan speed of 3. Within the hippocampal region, Iba1-positive microglia co-labeled with DAPI were randomly selected for imaging. The fluorescence signal threshold was set at 30% of the maximum fluorescence intensity, and areas exceeding this threshold were defined as regions of interest. Given that the *Pygl* RNA-FISH signal exhibits green fluorescence, the Analyze Particles function in ImageJ software was employed to quantify puncta per cell. Each randomly captured image was analyzed to identify and count microglia that satisfied the following criteria: positive for DAPI, positive for Iba1, and containing green fluorescent puncta reaching the 30% fluorescence intensity threshold[25-27].

2.8. *Cell cultures, transfection, and Aβ treatment*

Poly-L-lysine-coated culture flasks were prepared by incubation for 12 h and rinsed with PBS. Surgical instruments required for the experiments were immersed in 75% ethanol for 12 h, air-dried, and sterilized by autoclaving for subsequent use. On the experimental day, Sprague Dawley rats aged 1−2 days postpartum were selected. The animals were disinfected by immersion in 75% ethanol for 2 min before removal. Under a sterile cell culture hood, the skin and skull of the pups were incised to expose the brain tissue. The brain tissue was extracted using forceps and placed in pre-cooled DMEM, then transferred to another sterile hood where the meninges were carefully removed with sterile ophthalmic forceps. The tissue was minced, and 10 mL of DMEM supplemented with 5 μL of DNase I (50 μg/μL) and 2 mL of 0.25% trypsin was added for digestion in an incubator for 15 min. FBS was added to terminate digestion, followed by centrifugation at 100×*g* for 5 min at 4 °C. After centrifugation, DMEM complete medium was added in three steps of 15 mL each, with gentle pipetting ten times and a 2 min settling interval after each addition. The supernatant was collected, filtered through a 70 μm strainer into a new centrifuge tube, mixed thoroughly, and seeded into pre-coated and rinsed culture flasks for incubation. The culture medium was refreshed every 2 days. The culture medium was refreshed every 2 days. After 1 week, the microglia were separated by shaking at 10×*g* for 5 h, exploiting their weaker adherence. The harvested primary microglia were assessed for purity *via* IBA1 immunocytochemical staining and flow cytometry. Furthermore, all procedures for microglial culture and isolation followed standardized protocols[16,28,29], and purity was consistently verified (Supporting Information Fig. S1). Primary astrocytes were isolated and cultured using the same initial method as microglia, but due to their strong adherence, they were subcultured and purified *via* trypsinization. Primary neurons were isolated following the same initial protocol as microglia, but were cultured in neurobasal medium supplemented with B27 for 14 days, with half-medium changes every 2 days.

The human microglial cell line HMC3 was purchased from Wuhan Procell Life Technology Co., Ltd. (Wuhan, China) and had been authenticated and tested negative for mycoplasma contamination. The human microglial cell line HMC3 was cultured in DMEM containing 10% FBS, 1% sodium pyruvate, and 1% penicillin/streptomycin. All cells were cultured in a constant temperature incubator at 37 °C with 5% CO_2.

For knockdown experiments, siRNA was transfected into microglia using Lipo3000 in Opti-MEM for 12 h, followed by medium replacement and a further 12-h incubation. For the overexpression studies, plasmids were transfected using Lipo3000 and P3000 in Opti-MEM for 6 h, then replaced with complete medium and cultured for 12 h before subsequent experiments. Aβ was purchased from Qyaobio (Shanghai, China), and the cells were treated with different concentrations for 12 h. In the experimental results, Aβ represents oligomerized Aβ_{42}. Moreover, thorough biophysical and toxicological characterization of Aβ_{42} was performed *via* Western blot and transmission electron microscopy, supported by literature[30-32], confirming the oligomeric

state of the commercially obtained Aβ_{42}, which was further validated experimentally (Supporting Information Fig. S2).

2.9. Cell immunofluorescence and HiLyte-Aβ_{42} phagocytosis assays

The cells were seeded onto pre-coated coverslips in culture wells and treated with the indicated drugs. After treatment, the cells were washed with PBS and fixed with 4% paraformaldehyde for 15 min at room temperature. Fixed cells were permeabilized with 0.1% Triton X-100 for 5 min to enhance membrane permeability. Subsequently, nonspecific binding was blocked with 5% BSA for 1 h before incubating with primary antibodies overnight at 4 °C. The next day, the cells were washed three times with PBST and incubated with fluorescently labeled secondary antibodies for 1 h at room temperature in the dark. Nuclei were counterstained with DAPI, and coverslips were mounted for observation and image acquisition using a fluorescence microscope. For the phagocytosis assay, primary microglia were seeded in 24-well plates. After treatment, the cells were washed with PBS and incubated with 10 μL HiLyte Fluor™ 488-Aβ_{42} per well for 6 h in the dark. The cells were subsequently processed according to standard immunofluorescence staining procedures. Finally, the DAPI-stained samples were mounted and examined by fluorescence microscopy. HiLyte-Aβ_{42} was obtained from Anaspec (cat. AS-60479-01, CA, USA). This reagent has been widely utilized to evaluate the phagocytic capacity of microglia for Aβ_{42}[16]. Further characterization of HiLyte-Aβ_{42} *via* transmission electron microscopy confirmed its oligomeric properties (Supporting Information Fig. S2). Moreover, it is broadly recognized and validated for assessing Aβ_{42} phagocytic activity in cellular experimental systems[33,34].

2.10. Glycogen content assay

Tissues or cell lysates were homogenized, and the protein concentrations were determined from 50 μL aliquots. The samples were washed with cold PBS, resuspended in 30% KOH, and heated for 2 h. Glycogen was precipitated with an equal volume of 95% ethanol before centrifuging and dissolving or resuspending the pellet in ddH_2O. Acidified samples were reprecipitated with ethanol. The glycogen content was measured using commercial assay kits, with fluorescence read at E_x/E_m = 535 nm/587 nm, and normalized to protein content.

2.11. Periodic acid-schiff (PAS) staining

The PAS staining was measured using PAS staining kits according to the manufacturer's instructions. Briefly, after treatment, cells were fixed for 15 min with the kit-provided fixative, washed thoroughly, and air-dried. An oxidizing reagent was applied at room temperature, followed by washing. Schiff reagent was added in the dark and washed with running water for 5 min. PAS-stained samples were imaged using an optical microscope (Leica, Wetzlar, Germany), ensuring consistent magnification and illumination intensity across all samples. PAS staining intensity reflects glycogen content. Therefore, we assessed PAS staining intensity with ImageJ software by applying a consistent threshold range to all images, which provided a grayscale value for each pixel[35,36].

2.12. Transmission electron microscopy

Tissues or cells were collected and fixed in 2.5% glutaraldehyde at 4 °C. Following primary fixation, samples were rinsed three times with PBS for 15 min each. The samples were then transferred to 1% tannic acid for secondary fixation and washed thoroughly before dehydration. Dehydration was performed using a graded ethanol series (30%, 50%, 70%, 80%, 90%, and 100%, 20 min each), followed by complete dehydration in pure acetone. The dehydrated samples were infiltrated with epoxy resin, embedded, and then polymerized at 60 °C for 48 h. The polymerized samples were sectioned into ultrathin slices (70−90 nm) and mounted onto copper grids for staining. Ultrathin sections were stained with 2% uranyl acetate for 15 min, followed by 0.5% lead citrate for 10 min. After air-drying, the samples were examined using a transmission electron microscope. The ultrastructure of microglia was analyzed using a Hitachi transmission electron microscope (80 kV). The identification of microglia and their cytoplasmic content was previously described in detail[37]. Typical microglia were identified by their heterochromatic nuclei and distinguished from oligodendrocytes by their elongated endoplasmic reticulum profiles and the presence of diverse, heterogeneously dispersed cytoplasmic inclusions, such as lysosomes and lipofuscin granules. Glycogen granules were classified based on their typical electron-dense, spherical appearance and a diameter ranging from 22 to 40 nm, consistent with established ultrastructural descriptions of β-glycogen particles in the brain. To minimize false-positive identification, a threshold of more than five granules per cell was used to define a microglia as glycogen-positive[37]. Additionally, for transmission electron microscopy sample preparation of oligomerized Aβ_{42} and HiLyte-Aβ_{42}, a 10 μL aliquot of each sample was first applied onto a copper grid and allowed to settle for 1 min. Excess liquid was then removed using filter paper. Subsequently, 10 μL of uranyl acetate was applied to the grid and allowed to settle for 1 min, after which the excess staining solution was removed with filter paper. The grid was then air-dried at room temperature for 5 min. Imaging was performed using a transmission electron microscope operated at 80 kV and 10 μA.

2.13. Enzyme-linked immunosorbent assay (ELISA)

For the detection of soluble Aβ_{40} and Aβ_{42} levels, brain tissue was homogenized in cold PBS containing 5% BSA, 0.03% Tween-20, and protease inhibitor cocktail, followed by centrifugation at 16,000×*g* for 20 min at 4 °C, with the supernatants collected for analysis. To detect insoluble Aβ_{40} and Aβ_{42} levels, the resulting pellet was resuspended in PBS containing 1% Triton X-100 and protease inhibitors, followed by ultracentrifugation at 100,000×*g* for 1 h at 4 °C. The pellet was then resuspended in 70% formic acid (F112038, Aladdin, Shanghai, China) and subjected to ultracentrifugation at 100,000×*g* for 1 h at 4 °C. The supernatant was then neutralized with a formic acid neutralization buffer (1 mol/L Tris base, 0.5 mol/L Na_2HPO_4, 0.05% NaN_3) prior to quantification[38-40]. Aβ_{40} and Aβ_{42} levels were measured using ELISA kits according to the manufacturer's instructions, and absorbance was measured using a microplate reader.

2.14. mCherry-eGFP-LC3 adenovirus infection

Primary microglial cells in good condition were seeded into 24-well plates. The cells were infected with mCherry-eGFP-LC3 adenovirus at a final concentration of 1×10^9PFU/mL (MOI = 80). The virus was mixed with complete culture medium before being added to the cells. After 4 h of infection, half of the medium was replaced with fresh culture medium. 12 h post-infection, the viral medium was removed, and the cells were

washed once with PBS and replaced with fresh complete medium before being maintained at 37 °C in a 5% CO_2 incubator. At 36 h post-infection, microglial cells showed optimal fluorescent protein expression and maintained good viability. The cells were then processed for subsequent fixation, mounting, and fluorescence imaging.

2.15. Flow cytometry

Primary microglial cells were seeded into 24-well plates and allowed to reach approximately 60% confluence before drug treatment. After washing with PBS, 10 μL of HiLyte Fluor™ 488-Aβ_{42} was added to each well and incubated for 1 h. The cells were collected by centrifugation, the supernatant was discarded, and the cells were incubated with a pre-prepared flow cytometry antibody cocktail at 4 °C for 30 min. Following incubation, the cells were washed by centrifugation, resuspended in PBS, and subjected to flow cytometry analysis using FlowJo software. For live cell sorting, mice were anesthetized *via* intraperitoneal injection and perfused with PBS. The hippocampus was dissected and minced in ice-cold HBSS. Brain tissue was homogenized in medium containing 2% FBS, followed by digestion with 0.5 mg/mL collagenase IV and 10 U/mL DNase I at 37 °C for 15−20 min. The cell suspension was filtered, resuspended in 70% Percoll, and then subjected to density gradient centrifugation at 500×*g* for 20 min. The intermediate cell layer was collected, washed twice with PBS, and resuspended in PBS containing 2% FBS. Fluorescently labeled antibodies and a fixable viability dye were added and incubated at 4 °C in the dark for 30 min. The cells were finally resuspended in staining buffer and immediately processed for flow cytometric sorting.

2.16. RNA-seq and Smart-seq

After drug treatment, the cells were collected *via* centrifugation, but the supernatants were discarded. The cell pellets were lysed in TRIzol reagent and stored at −80 °C for transcriptomic sequencing. The RNA concentrations were determined to ensure quality control before sequencing. Sequencing was performed by LC-Bio Technologies (Hangzhou, China) Co., Ltd., using an Illumina platform, and gene expression matrices were obtained. Principal component analysis (PCA) was used to exclude batch effects among samples. Differentially expressed genes (DEGs) were identified using the limma package, with thresholds of $P< 0.05$ and $|\mathrm{Log_2FC}| > 0.5$. Protein−protein interaction networks were analyzed using the STRING database (https://cn.string-db.org/), and pathways with $P< 0.05$ were visualized as bubble plots. For Smart-seq of the hippocampal microglia, mice were anesthetized *via* intraperitoneal injection and perfused with HBSS. The hippocampus was dissected under sterile conditions and digested in brain dissociation medium (DMEM supplemented with type IV collagenase, DNase I, and FBS) at 37 °C and 20×*g* for 1 h. The digestion was terminated with EDTA, and the cell suspensions were centrifuged at 4 °C and 100×*g* for 10 min. The cells were resuspended in staining buffer, filtered, and subjected to density gradient centrifugation using 37% and 70% Percoll at 500×*g* for 25 min. The intermediate cell layer was collected, washed with staining buffer, and centrifuged again. After staining with fluorescent antibodies and fixable viability dye for 10 min, live microglia were isolated by fluorescence-activated cell sorting. The sorted cells were lysed in TRIzol and stored at −80 °C until Smart-seq transcriptomic sequencing. Quality control, library preparation, sequencing, and downstream analyses were conducted as described above.

2.17. Untargeted metabolomics

Cells were collected after drug treatment and stored at −80 °C for subsequent analysis. For extraction, 200 μL of methanol was added, and the samples were vortexed. The cells underwent three freeze−thaw cycles using liquid nitrogen and were vortexed between cycles to ensure complete lysis. After centrifugation at 16,100×*g* for 3 min at 4 °C, the supernatants were transferred and allowed to stand for 30 min. Following another round of centrifugation (16,100×*g*, 3 min, 4 °C), the supernatants were collected and combined with 80% methanol in water containing internal standards. The mixture was vortexed to ensure complete suspension and then centrifuged at 16,100×*g* for 3 min at 4 °C. The supernatants were transferred for analysis. Metabolite profiling was performed using a UPLC−MS/MS platform, and data were processed using Analyst 1.6.3 software. PCA was used to assess metabolite variance and correct for batch effects. Orthogonal partial least squares discriminant analysis was used to remove unrelated variation and improve group separation. Differential metabolite analysis was conducted using MetaboAnalystR (R software), with metabolites with $|\mathrm{Log_2FC}| > 0.5$ and $P< 0.05$ considered significant. Pathway enrichment and visualization of differential metabolites were performed using the RaMP-DB method and Cytoscape software.

2.18. Extracellular acidification rate (ECAR)

The ECAR of microglia was measured using a SeaHorse XF96 analyzer. Cells at 50%−60% confluence were treated as indicated and exposed to sequential injections of 10 mmol/L glucose, 2 μmol/L oligomycin, and 50 mmol/L 2-deoxy-D-glucose. Real-time ECAR was recorded to evaluate glycolytic capacity.

2.19. Sample preparation and analysis by UHPLC-HRMS/MS

LC-MS grade acetonitrile, methanol, and ammonium acetate were purchased from ANPEL Laboratory Technologies (Shanghai, China). For ^{13}C tracing experiments, Primary microglial cells were first transfected with siRNA for 48 h, followed by concurrent treatment with Aβ_{42} and 2 g/L U-^{13}C6-glucose (Cambridge Isotope Laboratories, CLM-1396-MPT). After 12 h of treatment, the medium was aspirated, and cells were rapidly washed three times with pre-chilled PBS to remove residual medium and exogenous metabolites. Subsequent metabolite extraction was performed immediately, with all steps conducted on ice to minimize metabolic activity. Sample preparation and analysis were conducted by ProfLeader Biotech (Shanghai, China) using the following protocol. Cells in the dish were scraped in 500 μL of cold extraction reagent (acetonitrile/methanol/water, 4:4:2, *v*/*v*/*v*) including internal standards, and processed with an ice-water bath for 5 min. After centrifugation at 16,000×*g* and 4 °C for 15 min, the supernatant was collected and dried under a gentle nitrogen. The dry extracts were reconstituted in 50 μL of 50% aqueous acetonitrile before UHPLC−HRMS/MS analysis. Sample analysis was performed on a Vanquish UHPLC system coupled to an Orbitrap Fusion Lumos Mass Spectrometer (Thermo Fisher Scientific). The redissolved extracts (2 μL) were injected into an Acquity UPLC BEH Amide column (100 mm × 2.1 mm, 1.7 μm, Waters Corporation) at a flow rate of 0.3 mL/min with mobile

phase (A) water and (B) 90% acetonitrile, both with 15 mmol/L ammonium acetate (pH = 9). A linear gradient elution was started from 90% B and held for 1 min, decreased to 75% B at 9 min, to 50% B at 10 min, and held for 12 min, finally returned to 90% B at 12.1 min and equilibrated for 14 min. The eluted metabolites were ionized in the negative mode of Heated Electrospray Ionization. Spray voltage was set to 2500 V. Ion Transfer Tube Temp and Vaporizer Temp were 325 and 450 °C, respectively. Sheath Gas was 40 (Arb, arbitrary unit), and Aux Gas was 10 (Arb). The full scan was operated at a mass resolution of 60,000 at a range of *m/z* 100−700. Simultaneously, the fragment ions information of the top 10 precursors in each scan was acquired at a mass resolution of 15,000 by data-dependant acquisition with HCD energy at NCE 15, 30, and 45, respectively. For the detection of Free G6P, Free glucosamine, Free UDP-GlcNAc, and glycogen-derived glucosamine, primary microglial cells were washed three times with ice-cold PBS following siRNA transfection and Aβ_{42} treatment. Metabolites were then extracted using methanol/water/chloroform (volume ratio 2:1.5:1), and the mixture was separated into polar (aqueous layer), lipid (chloroform layer), and insoluble (protein/glycogen) fractions. The polar (aqueous) layer was used to determine the relative abundance of Free G6P, Free glucosamine, and Free UDP-GlcNAc. The insoluble fraction was further processed to separate glycogen from protein. Glycogen was isolated from the protein precipitate using 1.5 mL of ice-cold 10% trichloroacetic acid. The resulting protein fraction was treated with amylase and tested for glucose release to confirm complete glycogen removal. The isolated glycogen was dried in a vacuum centrifuge at 10^{-3} mBar, resuspended in deionized water, and further purified by density displacement through a 4%−20% sucrose gradient. Following glycogen isolation, Glycogen-derived glucosamine was released by acid hydrolysis according to previously described methods[41], and the resulting products were analyzed *via* a UHPLC−HRMS platform. Data acquisition and analysis were performed using Thermo Fisher Scientific Xcalibur software (version 4.0.27.19). Target ions and their isotopic peaks were extracted within a 10 ppm mass window based on extracted ion chromatograms. Peak areas for all metabolites were automatically integrated and manually reviewed to ensure integration accuracy. The integrated area of each compound was used to calculate relative abundance, with normalization to internal standards to correct for inter-sample variability.

2.20. NADPH/NADP$^+$ and GSH/GSSG

Cells were washed with PBS and centrifuged, and pellets were collected for protein quantification. NADPH/NADP$^+$ and GSH/GSSG ratios were determined using commercial kits and normalized to protein content.

2.21. Generation of the HMC3 SNAP29 CRISPR knockout (KO) cell line

The CRISPR/Cas9 system was used to generate a homozygous SNAP29 KO cell line using HMC3 cells. In brief, single guide RNA (sgRNA) oligonucleotides targeting human SNAP29 were designed, annealed, and cloned into the pSpCas9 (BB)-2A-Puro vector. The sgRNA-Cas9 plasmid was then amplified by PCR and transformed into competent cells. Plasmid DNA was purified using a GeneJet Plasmid Miniprep Kit according to the manufacturer's protocol. For transfection, plasmids were introduced into HMC3 cells using Lipo3000 and P3000 reagents in the appropriate culture medium according to the manufacturer's instructions. After single-cell clones were established, the cells were continuously cultured, and the successful SNAP29 knockout was verified by Western blot analysis.

2.22. Western blotting and Co-IP

Proteins from tissues and cells were extracted using RIPA buffer supplemented with protease inhibitors, quantified, and denatured in 5 × SDS-PAGE loading buffer at 100 °C for 10 min. For *O*-GlcNAc detection, cells were lysed in a buffer containing 50 mmol/L Tris−HCl (pH 7.4), 2 mmol/L EDTA, and 300 mmol/L NaCl, supplemented with protease inhibitors, phosphatase inhibitors, and OGA inhibitors (Thiamet G), followed by incubation for 30 min. Proteins were resolved by 8%−12% SDS-PAGE and transferred to nitrocellulose membranes. After blocking, the membranes were sequentially incubated with primary antibodies and HRP-conjugated secondary antibodies. Protein bands were visualized and quantified using ImageJ, with β-actin as a loading control. For Co-IP, magnetic beads were pre-washed with IP lysis buffer containing protease and phosphatase inhibitors. Following treatment, cells were lysed on ice for 20 min, and supernatants were incubated overnight at 4 °C with the target antibody or IgG as a control. Immune complexes were captured using magnetic beads for 1 h at room temperature, washed extensively, and then eluted by boiling in 1 × SDS-PAGE loading buffer. Immunoblotting was performed as described above. For the OGA treatment assay, after obtaining the immunocomplex and prior to Western blotting, the samples were treated with 5 μg of recombinant OGA protein (Catalog No: HY-P79242, MCE, Shanghai, China) in a 200 μL reaction volume at 37 °C for 2 h. Subsequently, the samples were mixed with 1 × SDS-PAGE loading buffer, boiled, and subjected to Western blot analysis[42]. The primary antibodies used were as follows: PYGL (rabbit, 1:1000), PYGM (rabbit, 1:1000), PYGB (rabbit, 1:1000), P62 (rabbit, 1:5000), LC3 (rabbit, 1:3000), *O*-GlcNAc (rabbit, 1:1000), HA/Myc/Flag (rabbit), and β-actin (rabbit, 1:5000). HRP-conjugated secondary antibodies (anti-mouse and anti-rabbit, 1:1000) were obtained from Bioworld. Secondary antibodies that do not recognize light or heavy chains were purchased from Abcam.

2.23. qRT-PCR

After washing the cells and tissue samples with PBS, an appropriate volume of FreeZol Reagent was added, and the samples were vortexed thoroughly. The samples were then incubated at room temperature for 5 min to allow complete lysis. Dilution Buffer was added to the lysate, mixed well, and centrifuged to separate the aqueous phase. Isopropanol was then added to precipitate the RNA, followed by centrifugation to collect the white RNA pellet, which was washed with 95% ethanol and air-dried at room temperature. Finally, the RNA was dissolved in DEPC-treated water, and its concentration was measured before qRT-PCR analysis. Finally, we used the $2^{-\Delta\Delta CT}$ method with three biological replicates of samples to calculate the relative gene expression, with β-actin serving as the control. The primers used in this research are shown in Supporting Information Table S3.

2.24. Bioinformatic analysis

The GSE33000 dataset, comprising gene expression data from the prefrontal cortex of 310 patients with AD and 157 healthy

controls, was obtained from the Gene Expression Omnibus database at the National Center for Biotechnology Information. Quality control and differential gene expression analyses were performed using GEO2R. Reactome pathway enrichment analysis was then conducted on the DEGs, with metabolic pathways extracted and visualized as bubble plots. A heatmap was generated for glycogen metabolism-related genes within the GSE33000 dataset. Differential expression analysis of microglia located near and distant from Aβ plaques in the GSE101689 dataset was also performed, followed by Reactome pathway enrichment analysis and heatmap visualization of glycogen metabolism-related genes. Adjusted *P*-values <0.05 were considered statistically significant. To assess the relationship between *Pygl* mRNA expression and cognitive function, data from the prefrontal cortex of individuals with and without cognitive impairment ($n = 35$) in the GSE185909 dataset were analyzed using Pearson correlation with Mini-Mental State Examination scores. Correlation coefficients with $|r| > |\pm 0.3|$ and $P < 0.05$ were considered statistically significant.

2.25. Statistical analysis

Unless otherwise specified, all data are expressed as the mean ± standard deviation (SD). Statistical analyses were performed using GraphPad Prism software (version 9.0). For comparisons between two independent groups, normality was assessed using the Shapiro−Wilk test. If data followed a normal distribution with homogeneity of variance, a two-tailed unpaired Student's *t*-test was applied. If data were normally distributed but variances were unequal, Welch's *t*-test was used. For comparisons involving multiple groups under a single-factor intervention, one-way or two-way analysis of variance (ANOVA) was performed. If ANOVA revealed a significant overall difference, Tukey's multiple comparisons test was subsequently conducted for pairwise comparisons to control for type I error. All experiments described in this study were performed using a minimum of three mice or independent replicates. A *P*-value <0.05 was considered statistically significant, with significance levels denoted as follows: $^{*}P < 0.05$, $^{**}P < 0.01$, $^{***}P < 0.001$, and $^{****}P < 0.0001$.

3. Results

3.1. Aberrant glycogen catabolism in microglia during AD progression

To investigate the characteristics of glycogen metabolism in the brain during AD progression, we first examined glycogen levels in the hippocampal tissues of patients with and without AD. Compared with non-AD controls, patients with AD exhibited a marked increase in glycogen levels in the hippocampus (Fig. 1A). Similarly, starting at 7 months of age, AD mice showed elevated glycogen levels in the cortex and hippocampus compared with age-matched WT mice, with this increase persisting and intensifying alongside disease progression (Fig. 1B and C). Next, we identified DEGs and conducted pathway enrichment analyses using bioinformatics analyses of transcriptomic data from AD and non-AD brain samples. In addition to the metabolic pathways of lipid, cholesterol, and amino acids, which are rich in nutrients[13,43,44], we found significant enrichment of glycogen metabolism and glycogenolysis processes that have received limited attention in the context of AD (Fig. 1D). Differential expression analysis revealed significant upregulation of key enzymes involved in glycogen metabolism, including *PGM2*, *GYG2*, *GYS1*, *PYGL*, *PYGM*, *GAA*, and *PYGB*, while *AGL* was downregulated in AD brains compared with controls (Fig. 1E). These findings suggest that AD pathology is accompanied by aberrant glycogen metabolism in the CNS.

Critically, using transmission electron microscopy[37], we observed a significant increase in the number of glycogen granules in the hippocampal microglia from AD patients compared to non-AD individuals (Fig. 1F and G). To confirm this finding, we used biological glycogen probes to examine glycogen content in hippocampal microglia at different pathological stages in AD mouse models[24,45]. Our results revealed that AD mice exhibited an increased number of glycogen granules in microglia compared with age-matched WT mice, with this increase being particularly pronounced in older AD mice (Fig. 1H and I). These findings suggest that microglia undergo aberrant glycogen metabolism during AD progression. Next, we isolated microglia from the hippocampus of 10-month-old WT and AD mice by using a fluorescence-activated cell sorter (Fig. 1J, Supporting Information Fig. S3A) and assessed the expression of key enzymes involved in glycogen metabolism. qRT-PCR analysis demonstrated that, relative to WT mice, microglia from AD mice exhibited significant upregulation of major glycogen metabolism enzymes, including *Gys1, Gys2*, *Pgm2*, *Pygl*, and *Ugp2*. Notably, among the three isoforms of glycogen phosphorylase, only *Pygl* was markedly upregulated, whereas *Pygb* and *Pygm* showed no significant changes (Fig. 1K). These data indicate that glycogen metabolism in microglia is profoundly altered during AD pathological progression. Furthermore, we extracted and cultured primary microglia from neonatal mice and examined the effects of Aβ treatment on glycogen metabolism. Transmission electron microscopy revealed that Aβ stimulation significantly increased the number of glycogen granules in primary microglia (Fig. 1L and M). Consistent with these findings, glycogen content assay kits and PAS staining confirmed elevated glycogen levels (Fig. 1N, Supporting Information Fig. S4A and S4B). Moreover, RNA-seq was performed to assess transcriptomic alterations in primary microglia following Aβ treatment. The enrichment results of reactome and gene ontology biological processes (GOBP) indicated that, after Aβ treatment, primary microglia were significantly enriched in processes such as glycogen metabolism, regulation of glycogen metabolism process, glycogen breakdown, glycogenolysis, and regulation of glycogen catabolic process (Fig. 1O and P, Fig. S4C and S4D). Key metabolic enzymes such as *Gys1* and *Pygl* were also upregulated at the mRNA level (Fig. 1Q). The above-mentioned results indicate that microglia undergo significant alterations in glycogen catabolism during AD progression.

3.2. Microglial PYGL expression exhibits a spatiotemporal correlation with pathological upregulation in AD

Glycogen exerts its biological functions primarily through degradation and subsequent metabolic pathways, a process mediated by glycogen phosphorolysis[21,46]. Among these enzymes, PYGL, PYGB, and PYGM represent distinct isoforms (Fig. 2A). Our previous results showed that both AD brain tissue and microglia upregulated *PYGL* mRNA expression. Interestingly, data from the human Brain-seq showed that microglia predominantly express *PYGL*, with an extremely low abundance of *PYGB* and *PYGM* (Fig. 2B). We confirmed this finding by analyzing primary microglia, astrocytes, and neurons, with Western blotting demonstrating that microglia indeed express significantly higher

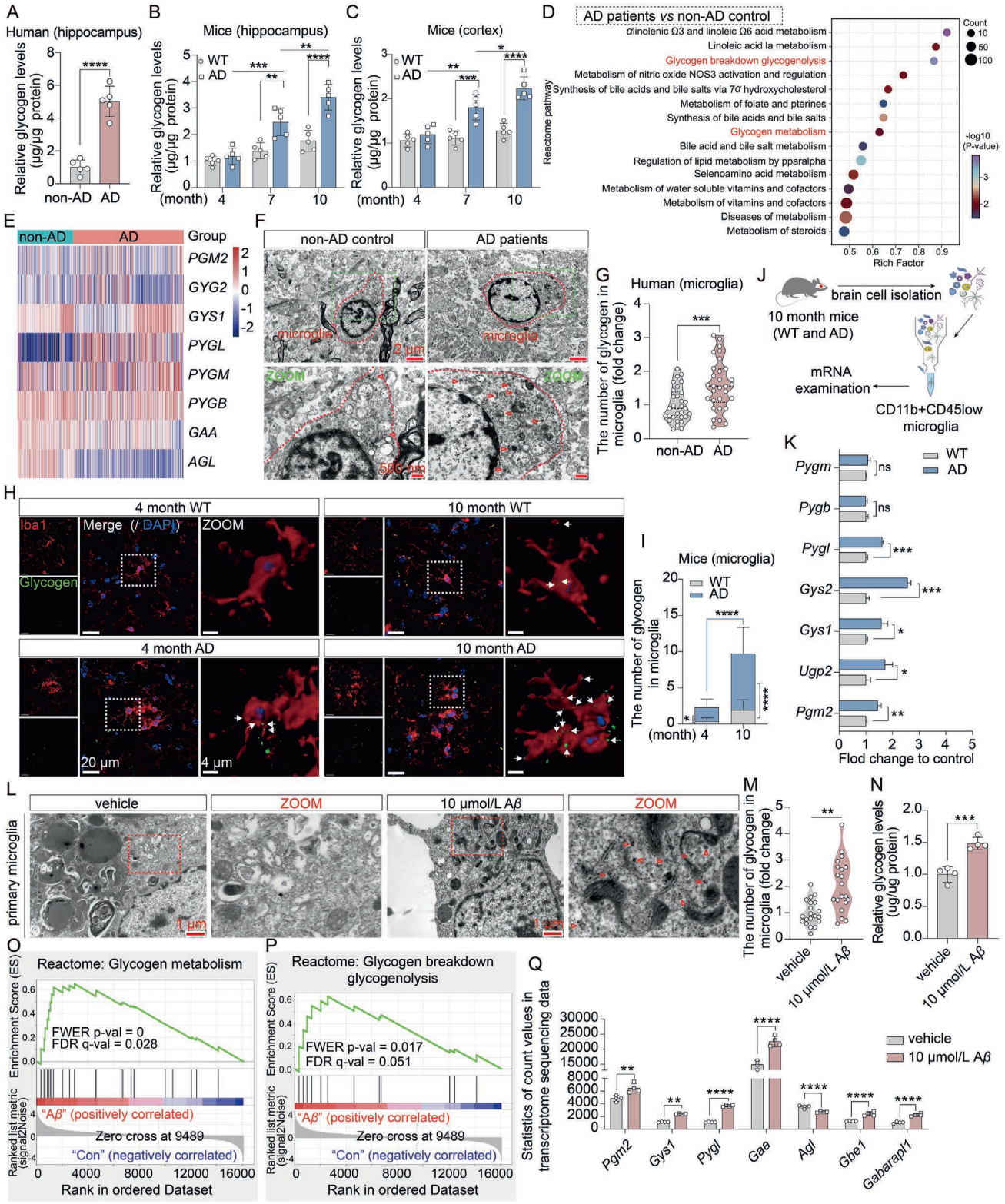

Figure 1 Aberrant glycogen catabolism in microglia during AD progression. (A) Quantification of glycogen levels in the hippocampus of patients with and without AD (n= 5 samples). (B) Quantification of glycogen levels in the hippocampus of WT and AD mice at 4, 7, and 10 months of age (n= 5 mice). (C) Quantification of glycogen levels in the cortex of WT and AD mice at 4, 7, and 10 months of age (n= 5 mice). (D) Enrichment analysis of metabolic pathways within the Reactome pathways based on differentially expressed genes between the brain transcriptomes of patients with and without AD in the GSE33000 dataset. (E) Heatmap showing the expression profiles of key glycogen metabolism-related genes with significant changes between the brains of patients with and without AD in the GSE33000 dataset. (F, G) Transmission electron microscopy was used to detect the number of glycogen granules in the hippocampal microglia from patients with and

levels of PYGL compared with astrocytes and neurons (Supporting Information Fig. S5A and S5B). Furthermore, correlation analysis between *PYGL* expression in the brains of patients with AD and their Mini-Mental State Examination scores revealed that *PYGL* expression was significantly positively associated with the severity of dementia in these patients (Fig. 2C). This strongly suggests that disease stage-associated upregulation of PYGL mediates microglial abnormal glycogenolysis in AD.

To further explore the characteristics of microglial glycogenolysis, we next investigated the spatiotemporal changes in microglial PYGL during AD progression. First, we assessed PYGL expression in the human hippocampus. Western blot results showed that PYGL expression was higher in the hippocampus of patients with AD compared with those without (Fig. 2D and E). We then examined PYGL expression in the hippocampus and cortex of WT and AD mice at different ages (Fig. 2F). The results showed that, compared with WT mice, 7 and 10-month-old AD mice exhibited significantly higher PYGL expression in the hippocampus and cortex, respectively. Furthermore, PYGL expression in the hippocampus of AD mice exhibited a disease course-related upregulation trend (Fig. 2G and H). Importantly, we isolated hippocampal microglia from 10-month-old WT and AD mice and found that, compared with WT mice, microglia from AD mice exhibited a significant upregulation of PYGL protein expression, with no changes in PYGB or PYGM expression (Fig. 2I and J), which is consistent with previous results. We also compared the expression of PYGL in the hippocampal microglia of WT and AD mice at different ages. The RNA-FISH results showed that, compared to age-matched WT mice, the number of *Pygl* mRNA puncta in hippocampal microglia of 4-month-old AD mice was slightly increased, although no statistical significance was observed. However, a significant increase in *Pygl* mRNA puncta was found in 10-month-old WT mice. Furthermore, compared with 4-month-old AD mice, the number of *Pygl* mRNA puncta in hippocampal microglia of 10-month-old AD mice was significantly higher (Fig. 2K and L). Immunofluorescence staining of the PYGL protein confirmed this observation (Fig. 2M and N). Dark microglia surrounding Aβ plaques are key microglial clusters that drive AD pathological progression and often exhibit marked metabolic alterations[37,47]. Next, in 10-month-old AD mice, we compared PYGL expression in microglia located around Aβ plaques with that distant from the plaques[37] (Fig. 2O). The results illustrated that microglia surrounding Aβ plaques expressed significantly higher levels of PYGL compared with those located farther away from the Aβ plaques (Fig. 2P and Q). Subsequently, we analyzed publicly available single-cell transcriptomic datasets of AD transgenic mouse brains and performed Kyoto Encyclopedia of Genes and Genomes (KEGG) pathway enrichment analysis on the DEGs[48]. Interestingly, we found that, compared with microglia far away from Aβ plaques, those in close proximity to Aβ plaques exhibited significant abnormalities in glycogen metabolism (Fig. 2R), along with marked upregulation of *Pygl* expression (Fig. 2S). Moreover, *in vitro* experiments demonstrated that Aβ treatment led to a dose-dependent increase in PYGL protein levels, without affecting the expression of PYGB or PYGM (Fig. 2T−W), compared with the solvent control. Collectively, these findings confirm that microglia upregulate the expression of the glycogenolytic enzyme PYGL during the progression of AD pathology. This suggests that the abnormal increase in microglial PYGL is a key driver of aberrant glycogenolytic metabolism in microglia, thereby contributing to AD progression.

3.3. Specific knockdown of PYGL in microglia ameliorates cognitive deficits and neuropathology in AD mice

To elucidate the functional role of microglial glycogenolysis in AD progression, an AAV was injected bilaterally into the hippocampus of 8-month-old mice to specifically knock down PYGL in the microglia. Behavioral and neuropathological assessments were performed at 9 months of age (Fig. 3A). First, the transduction efficiency of the AAV in microglia was verified by immunofluorescence (Fig. 3B), and $CD45^{+}CD45^{low}$ microglia were sorted by using a fluorescence-activated cell sorter, and the knockdown efficiency of PYGL in microglia was confirmed. As shown in Fig. 3C and D, compared to the AD + AAV-NC group, the expression level of PYGL in microglia from the AD + AAV-PYGL-cKD group was significantly reduced. Furthermore, our detection results indicated no significant changes in the expression of PYGB or PYGM. We then evaluated the effects of microglial PYGL knockdown on the memory and cognitive function of AD mice. In the Morris water maze test, compared with AD mice injected with AAV-NC, those injected with AAV-PYGL-cKD exhibited a significantly shorter escape latency to reach the target during training trials (Fig. 3E). Furthermore, AAV-PYGL-cKD-injected AD mice showed a significantly shorter latency for the first entry to the target (platform), an increased number of target entries, and a longer time spent in the target quadrant during the probe trial (Fig. 3F−H, Supporting Information Fig. S6A), indicating restored spatial learning and memory deficits. The groups showed no significant differences in swimming speed (Fig. S6B), ruling out possible effects of compromised motor ability. The NORT and FCT are also commonly used to assess memory and learning in mice[29]. In the NORT, AD mice with microglial PYGL knockdown showed a significantly higher recognition index for novel objects compared with control AD mice (Fig. 3I), indicating enhanced recognition memory. In the FCT, the knockdown of microglial PYGL significantly increased the freezing time during re-exposure to the fearful context in AD mice (Fig. 3J, Fig. S6C), suggesting that inhibiting PYGL delayed

without AD ($n=$ 10 per sample with $n=$ 3 samples/group, total $n=$ 30). (H, I) The number of glycogen granules in microglial cells in hippocampal microglia from 4- and 10-month-old WT and AD mice was detected by immunofluorescence ($n=$ 8 per sample with $n=$ 3 samples/group, total $n=$ 24). (J) Schematic diagram showing the workflow for isolating hippocampal microglia from 10-month-old WT and AD mice for qRT-PCR analysis. (K) mRNA expression levels of key glycogen metabolism enzymes in hippocampal microglia from 10-month-old WT and AD mice ($n=$ 3 independent experiments). (L, M) Transmission electron microscopy was used to detect the number of glycogen granules in primary microglia treated with Aβ ($n=$ 6−7 per sample with $n=$ 3 samples/group, total $n=$ 20). (N) Detection of the glycogen content in primary microglia treated with Aβ ($n=$ 4 independent experiments). (O, P) Reactome pathway enrichment analysis of RNA-seq data from primary microglia treated with Aβ. (Q) Count values of differentially expressed key glycogen metabolism-related genes in Aβ-treated primary microglia ($n=$ 4 independent experiments). Quantitative data are presented as the mean ± SD; ns $P>$ 0.05; *$P<$ 0.05; **$P<$ 0.01; ***$P<$ 0.001; ****$P<$ 0.0001.

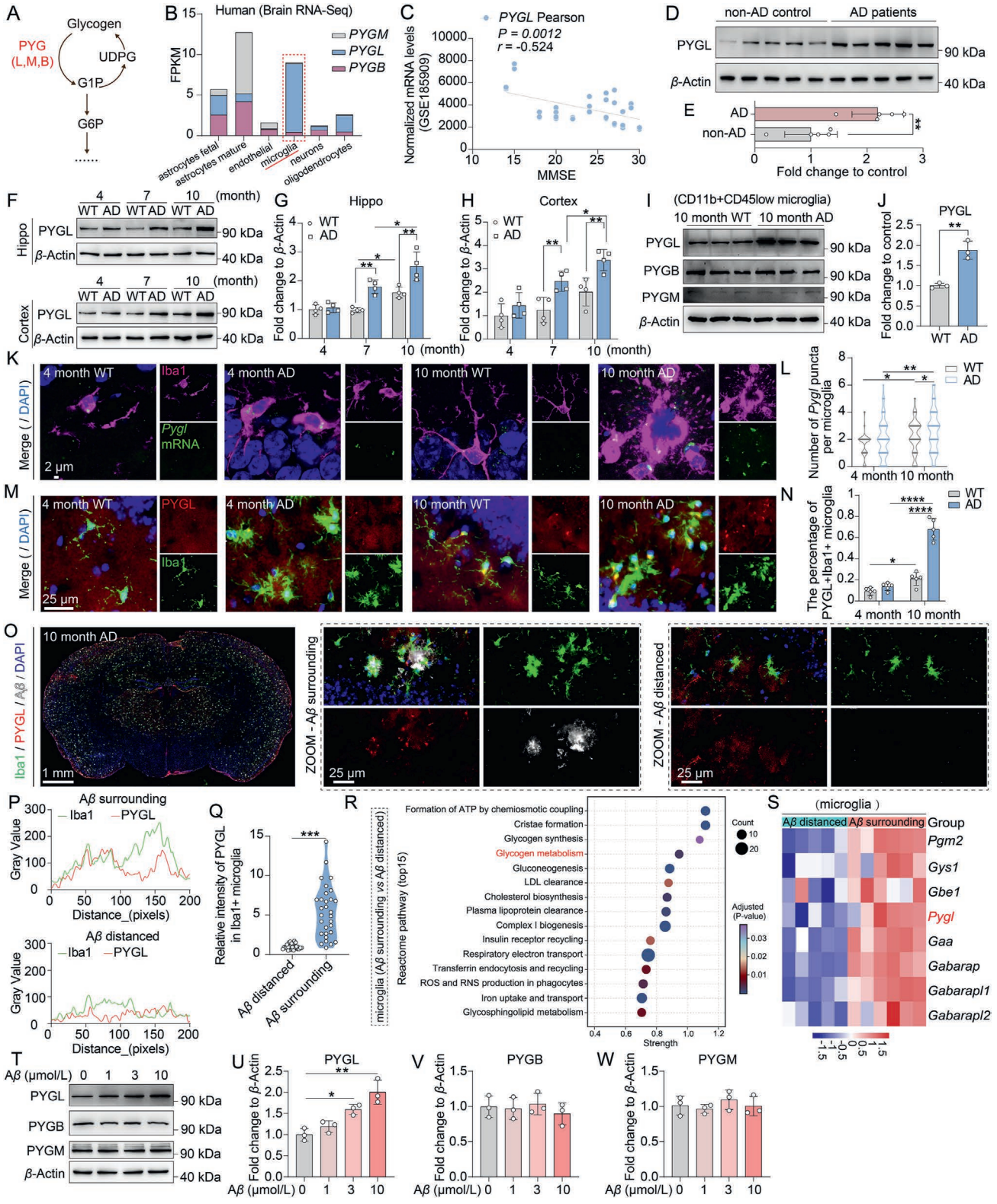

Figure 2 Microglial PYGL expression exhibits a spatiotemporal correlation with pathological upregulation in AD. (A) Schematic of the glycogen metabolism pathway. (B) FPKM values of *PYGM*, *PYGB*, and *PYGL* in different human brain cell types form the brain RNA-seq database (https://brainrnaseq.org/). (C) Correlation analysis between *PYGL* mRNA levels in brain tissue and Mini-Mental State Examination scores from patients in the GSE185909 dataset (n = 35 samples). (D) Protein levels of PYGL in hippocampal tissues from patients with and without AD. (E) Quantitative data shown in (D) (n = 5 samples). (F) Protein levels of PYGL in the hippocampus and cortex from WT and AD mice at 4, 7, and 10 months of age. (G, H) Quantitative data shown in (F) (n = 4 mice). (I) Protein levels of PYGL, PYGB, and PYGM in microglia isolated from the hippocampus of 10-month-old WT and AD mice. (J) Quantitative data shown in (I) (n = 3 independent experiments).

memory loss in these mice. Collectively, these behavioral results demonstrate that microglial PYGL knockdown restores the cognitive deficits of AD mice.

Next, we evaluated the effects of microglial PYGL knockdown on AD-related neuropathology. Immunofluorescence staining of the hippocampal region revealed that knockdown of microglial PYGL significantly reduced the number and area of Aβ plaques compared with AAV-NC (Fig. 3K−M). Furthermore, the ELISA results showed that knockdown of microglial PYGL decreased the levels of insoluble and soluble Aβ_{42} and Aβ_{40} in the hippocampus (Fig. 3N−Q). Given that neuroinflammation is a key neuropathological feature of AD, we next assessed the expression of pro-inflammatory cytokines in the hippocampus. The knockdown of microglial PYGL significantly reduced the mRNA expression levels of *Inos*, *Il1b*, *Il6*, *Tnfa*, and *Hmgb1* in the hippocampus of AD mice (Fig. 3R). Collectively, these results confirm that microglial PYGL knockdown alleviates AD-related neuropathology and improves cognitive function in mice with AD.

3.4. Knockdown of PYGL promotes microglial autophagosome−lysosome fusion to enhance Aβ clearance

To elucidate the functional role of PYGL in microglia, microglia were isolated from the hippocampi of AD mice injected with AAVs and then subjected to Smart-seq analysis (Fig. 4A). As shown in Fig. 4B, PCA revealed clear separation among the experimental groups, with high intra-group clustering consistency, underscoring the reliability of the data. Volcano plots illustrate the distribution of DEGs between the groups (Fig. 4C, Supporting Information Fig. S7A). In comparisons among AD mice, the AAV-PYGL-cKD group resulted in 461 upregulated and 408 downregulated genes in hippocampal microglia compared with the AAV-NC group (Fig. 4C). KEGG pathway enrichment analysis of these DEGs revealed significant enrichment of pathways including autophagy, IL-17 signaling, Toll-like receptor signaling, and TNF signaling in the AD + AAV-NC group relative to the WT + AAV-NC controls (Fig. 4D). Compared with the AD + AAV-NC group, microglia from the AD + AAV-PYGL group were predominantly enriched in pathways related to autophagy, mitophagy, NF-κB signaling, and phagosome (Fig. 4E). These data suggest that specific knockdown of PYGL predominantly alters autophagy, phagocytosis, and inflammatory activation processes in microglia during AD pathology. In addition, we extracted primary microglia and evaluated the impact of PYGL knockdown (Fig. S7B and S7C) on the biological function of microglia *via* RNA-seq *in vitro* experiments (Fig. 4F). The PCA results showed that the data quality of each experimental group was reliable and that the differences were significant (Fig. 4G). Volcano plots showed robust gene expression differences between groups (Fig. S7D and S7E). Compared with Aβ-treated primary microglia, the Aβ+ si-PYGL group displayed 616 upregulated and 809 downregulated genes (Fig. S7E). GOBP and KEGG pathway analyses further revealed that Aβ treatment significantly enriched pathways, including phagosome maturation, autophagy, IL-17 signaling, and lysosome processes, compared with the control (Fig. 4H). Notably, knockdown of PYGL in Aβ-treated primary microglia promoted enrichment of pathways related to regulation of autophagosome assembly, protein glycosylation, and metabolism compared with Aβ alone (Fig. 4I). Furthermore, the top ten enriched cellular component results indicated that autophagy/lysosome processes comprised 17.24% and 21.53% of the biological processes, respectively (Fig. 4J, Fig. S7F). Collectively, these findings suggest that PYGL knockdown may modulate microglial function in AD by regulating autophagy/lysosome pathways, phagocytic activity, and inflammatory responses.

Subsequently, we investigated the precise effects of PYGL intervention on autophagy in microglia. We first assessed LC3B expression in primary microglia. As demonstrated in Fig. 5A and B, Aβ exposure elevated LC3B protein levels, and knockdown of PYGL further increased LC3B expression, indicating that PYGL knockdown may enhance autophagy in Aβ-treated primary microglia. P62, an autophagy receptor protein, binds to LC3 to selectively sequester autophagic substrates into autophagosomes and is subsequently degraded by lysosomal proteases. Thus, its expression level is widely used to assess autophagic activity and flux integrity[49]. Western blot analysis showed that Aβ treatment increased both the LC3-II/I and P62 protein levels, whereas PYGL knockdown further elevated the LC3-II/I but reduced P62 protein expression (Fig. 5C and D). Microglia isolated from the hippocampus of 10-month-old WT and AD mice were analyzed by western blotting. Compared with the WT + AAV-NC group, microglia from the AD + AAV-NC group showed elevated LC3 II/I and increased P62 protein levels. PYGL knockdown further increased the LC3 II/I and reduced P62 levels (Fig. 5E and F), indicating enhanced autophagic flux in microglia following PYGL suppression. We employed a mCherry-eGFP-LC3 adenovirus to monitor autophagic flux in primary microglia. Due to the acid sensitivity of eGFP, autolysosome formation results in diminished green fluorescence and persistent red fluorescence, whereas blocked fusion events manifest as yellow puncta (Fig. 5G). Compared with the control, Aβ stimulation led to a marked increase in yellow puncta in primary microglia, suggesting impaired autophagosome−lysosome fusion. Knockdown of PYGL significantly decreased yellow puncta while increasing red puncta, demonstrating restoration of autophagic flux (Fig. 5H−J). Conversely, PYGL overexpression further impaired autophagic flux in microglia treated with Aβ (Supporting Information Fig. S8A−S8C). Together, these findings demonstrate that PYGL regulates autophagic flux by modulating autophagosomes−lysosomes fusion in microglia.

It has been proven that autophagy plays a crucial role in regulating microglial clearance of Aβ and pro-inflammatory

(K, L) RNA-FISH analysis showing the percentage of *Pygl* mRNA$^+$Iba1$^+$ microglia in the hippocampus of 4- and 10-month-old WT and AD mice ($n=$ 18 per sample with $n=$ 5 samples/group, total $n=$ 90). (M, N) Immunofluorescence analysis of PYGL$^+$ Iba1$^+$ microglia in the hippocampus of 4- and 10-month-old WT and AD mice ($n=$ 5 mice). (O−Q) Immunofluorescence analysis of PYGL expression in Iba1$^+$ microglia located surrounding or distant from Aβ plaques in the hippocampus of 10-month-old AD mice ($n=$ 10 per sample with $n=$ 3 samples/group, total $n=$ 30). (R) Metabolic pathway enrichment analysis of differentially expressed genes in Aβ surrounding *vs*. Aβ distanced microglia based on the GSE101689 dataset. (S) Heatmap showing key glycogen metabolism-related differentially expressed genes (DEGs) in Aβ surrounding *vs*. Aβ distanced microglia based on the GSE101689 dataset. (T) Protein levels of PYGL, PYGB, and PYGM in primary microglia treated with Aβ. (U−W) Quantitative data shown in (T) ($n=$ 3 independent experiments). Quantitative data are presented as the mean ± SD; *$P<$ 0.05; **$P<$ 0.01; ***$P<$ 0.001; ****$P<$ 0.0001.

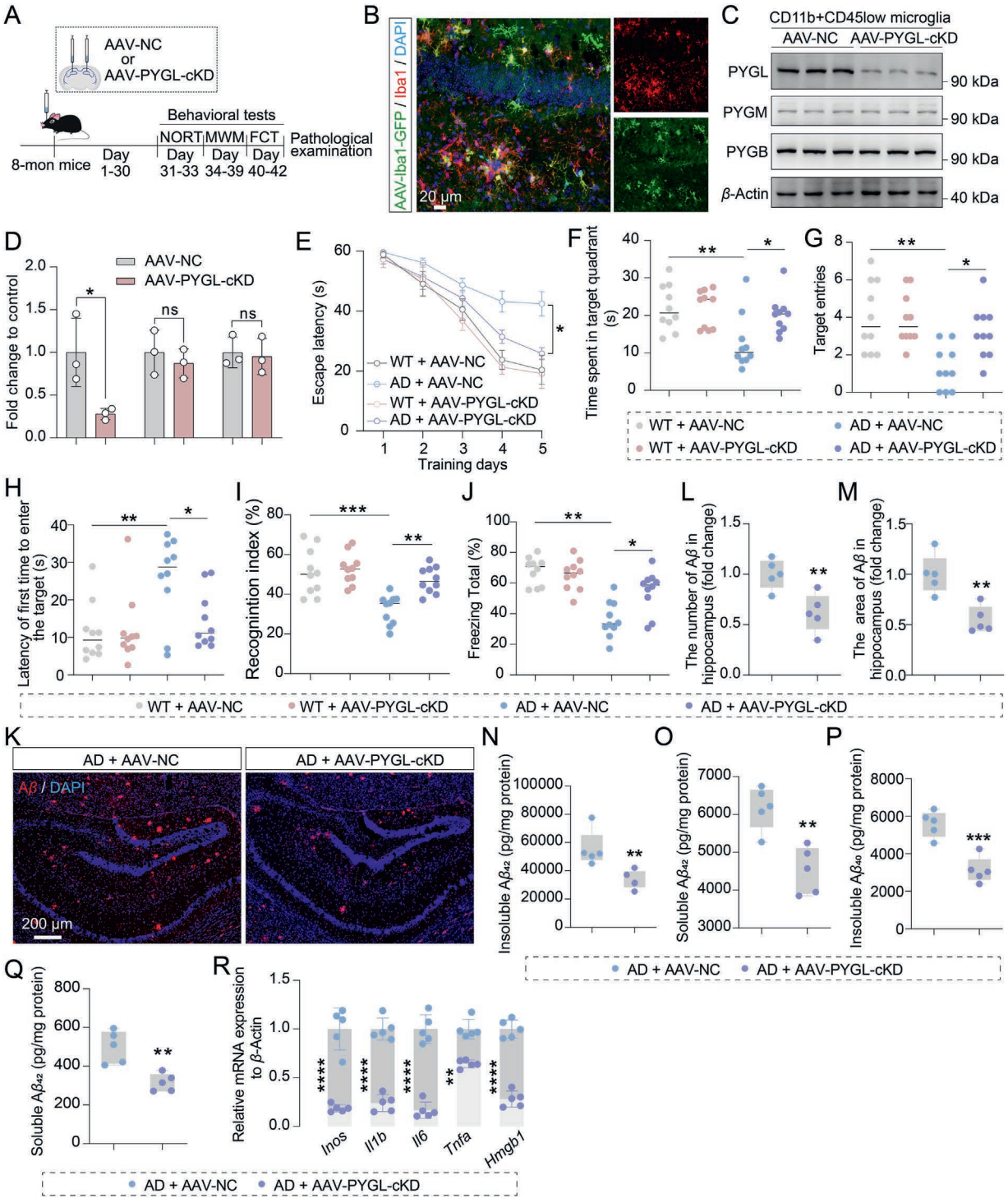

Figure 3 Specific knockdown of PYGL in microglia improves cognitive deficit and neuropathology in AD mice. (A) Schematic of adeno-associated virus (AAV) injection. Behavioral tests and pathological examinations were conducted. (B) Immunofluorescence showing the specificity of AAV injection in the hippocampus. (C, D) Protein levels of PYGL in $CD11b^{+}CD45^{low}$ microglia from 8-month-old mice were detected by conducting WB analysis ($n=$ 3 independent experiments). (E) Escape latency during the training trials of the Morris water maze ($n=$ 10 mice). (F−H) Behavioral performance in the probe trial of the Morris water maze, including time spent in the target quadrant (F), target entries (G), and latency to first target entry (H) ($n=$ 10 mice). (I) Recognition index assessed by the novel object recognition test (NORT) ($n=$ 10 mice). (J) Freezing time assessed by the fear conditioning test (FCT) ($n=$ 10 mice). (K) Immunofluorescence staining of Aβ deposits in the hippocampus following AAV injection. (L, M) Quantification of Aβ plaque number (L) and plaque area (M) in the hippocampus ($n=$ 5 mice). (N−Q) Enzyme-linked immunosorbent assay quantification of insoluble $A\beta_{42}$ (N), soluble $A\beta_{42}$ (O), insoluble $A\beta_{40}$ (P), and soluble $A\beta_{40}$ (Q) levels in the hippocampus of AD mice after AAV injection ($n=$ 5 mice). (R) mRNA levels of proinflammatory markers in the hippocampus of AAV-injected AD mice ($n=$ 5 mice). Quantitative data are presented as the mean ± SD; *$P<$ 0.05; **$P<$ 0.01; ***$P<$ 0.001; ****$P<$ 0.0001.

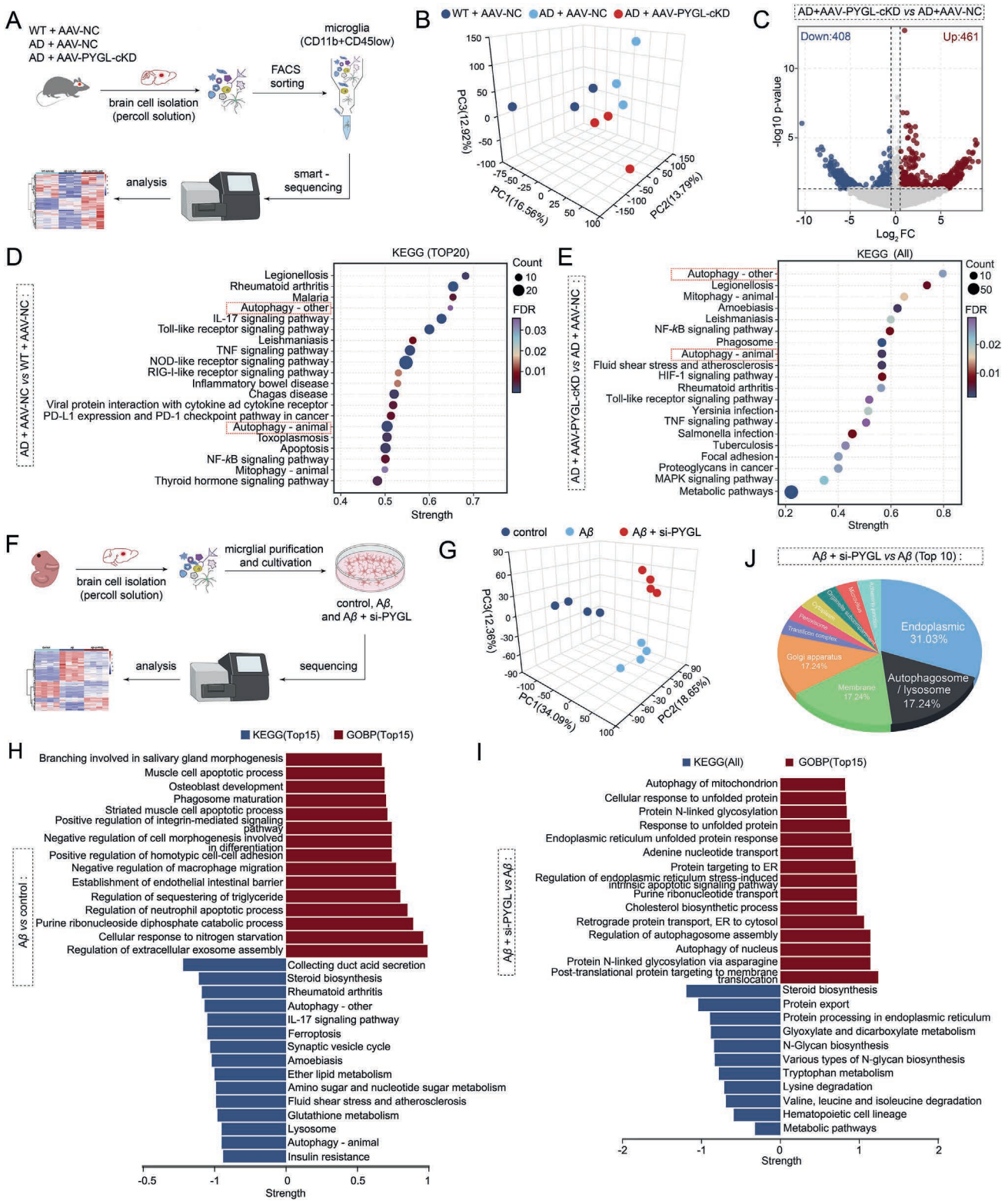

Figure 4 Knockdown of PYGL promotes microglial autophagosome−lysosome fusion to enhance Aβ clearance. (A) Schematic diagram of Smart-seq from microglia after AAV injection with flow cell sorting. (B) Principal component analysis (PCA) of microglial transcriptomes obtained by Smart-seq (n = 3 from 12 mice). (C) DEGs between AD + AAV-PYGL-cKD *vs*. AD + AAV-NC groups identified by Smart-seq. (D, E) Kyoto Encyclopedia of Genes and Genomes (KEGG) pathway enrichment of DEGs from Smart-seq comparing AD + AAV-NC *vs*. WT + AAV-NC (D), and AD + AAV-PYGL-cKD *vs*. AD + AAV-NC (E). (F) Schematic diagram of RNA-seq in primary microglia treated with Aβ and si-PYGL. (G) PCA of transcriptomic profiles from RNA-seq (n = 4 independent experiments). (H) Gene ontology biological processes (GOBP) and KEGG pathway enrichment of upregulated genes in Aβ *vs*. control groups. (I) GOBP and KEGG pathway enrichment of upregulated genes in Aβ+si-PYGL *vs*. Aβ groups. (J) Cellular component enrichment of upregulated genes in Aβ+si-PYGL *vs*. Aβ groups.

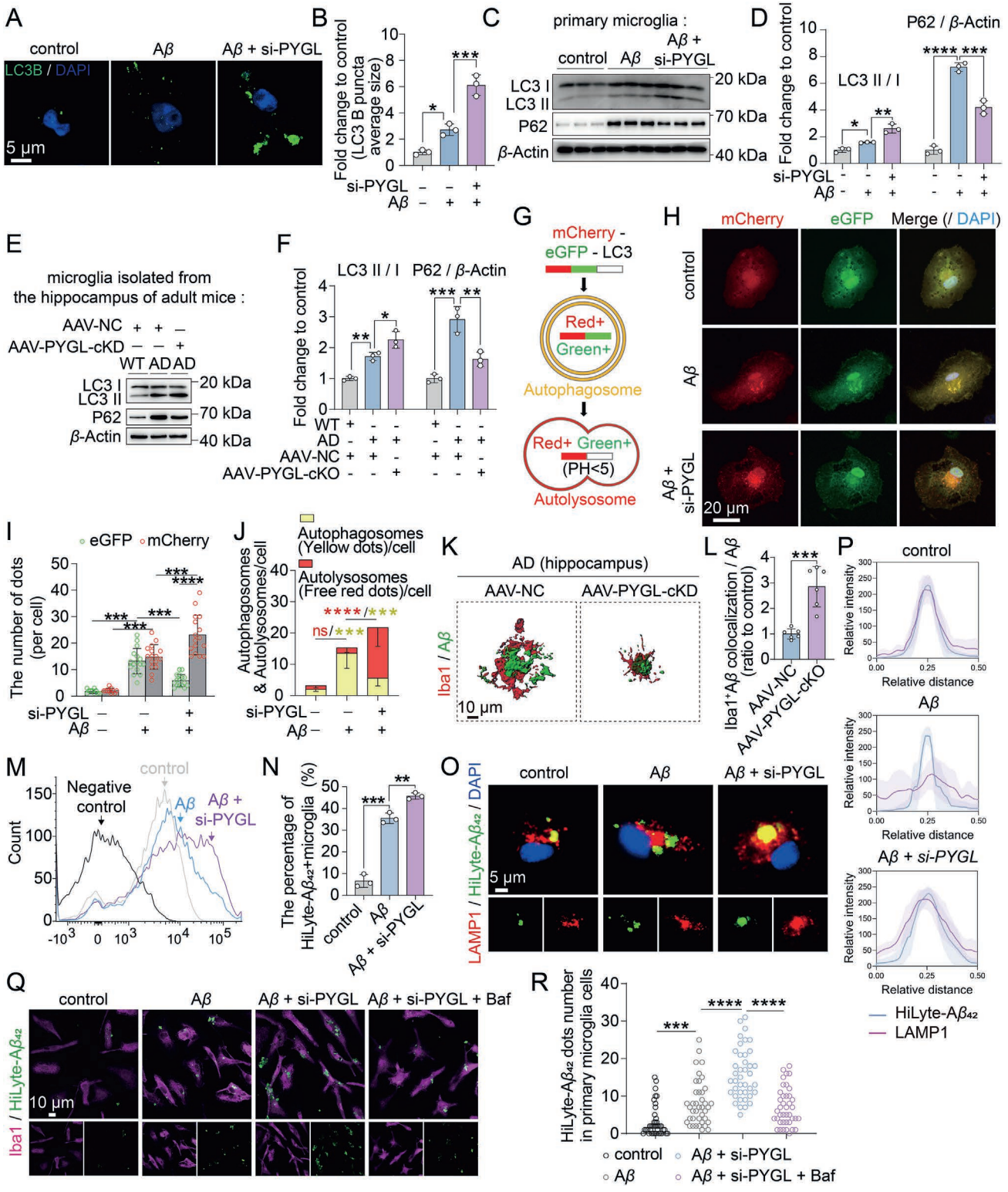

Figure 5 Knockdown of PYGL promotes microglial autophagosome−lysosome fusion to enhance Aβ clearance. (A) Immunofluorescence staining of LC3B in primary microglia treated with Aβ and si-PYGL. (B) Quantitative data of the fluorescent LC3B puncta, showing the average size of primary microglia in (A) ($n=$ 3 independent experiments). (C) Protein levels of LC3II/I and P62 in primary microglia treated with Aβ and si-PYGL. (D) Quantitative data shown in (C) ($n=$ 3 independent experiments). (E) Protein levels of LC3II/I and P62 in sorted microglia from AAV-injected mice. (F) Quantitative data shown in (E) ($n=$ 3 independent experiments). (G) Schematic diagram of mCherry-eGFP-LC3. (H−J) Immunofluorescence staining was used to quantify the number of dots (I), autophagosomes, and autolysosomes (J) per microglial cell in each group ($n=$ 5−6 per sample with $n=$ 3 samples/group, total $n=$ 16). (K) Immunofluorescence and 3D reconstruction of Aβ and Iba1 localization in the hippocampus after AAV injection. (L) Quantitative data showing fluorescence colocalization in (K) ($n=$ 6 mice). (M, N) Phagocytic

activation[50,51]. *In vivo* immunofluorescence staining demonstrated that microglial knockdown of PYGL enhanced microglial phagocytosis of Aβ (Fig. 5K and L). Consistently, *ex vivo* flow cytometry analysis revealed a significant increase in the proportion of primary microglia engulfing Hilyte-Aβ_{42} following PYGL knockdown under Aβ stimulation (Fig. 5M and N). Immunofluorescence analysis further showed that PYGL knockdown markedly promoted the colocalization of internalized fluorescent Aβ with lysosomes in primary microglia (Fig. 5O and P). These results confirm that PYGL inhibition facilitates microglial phagocytosis and degradation of Aβ. Moreover, PYGL overexpression suppressed microglial phagocytosis (Fig. S8D and S8E) and the degradation of engulfed Aβ (Fig. S8F and S8G). Bafilomycin A1, a specific inhibitor of autophagosome−lysosome fusion[52], abolished the enhanced Aβ phagocytosis induced by PYGL knockdown (Fig. 5Q and R), indicating that PYGL regulates microglial clearance of Aβ in an autophagy-dependent manner. In addition, PYGL knockdown reduced Aβ-induced mRNA expression of the pro-inflammatory cytokines *Tnfa*, *Il1b*, and *Il6* in primary microglia (Fig. S8H), while upregulating the anti-inflammatory markers *Arg1* and *Il10* (Fig. S8I). Overexpression of PYGL further promotes the pro-inflammatory response of microglia under Aβ stimulation (Fig. S8J). In addition, re-expressing PYGL reversed the effects induced by PYGL knockdown in microglia, which further confirms that the functional changes in microglia caused by PYGL knockdown are specifically mediated by PYGL (Fig. S8K−S8P). Collectively, these findings demonstrate that PYGL knockdown promotes autophagosome−lysosome fusion in microglia, thereby enhancing autophagic activity and facilitating Aβ clearance.

3.5. Knockdown of microglial PYGL suppresses HBP metabolism to reduce O-glycosylation levels

Metabolites generated from glycogen catabolism catalyzed by PYGL can enter multiple downstream pathways depending on enzymatic reactions, including glycolysis, PPP, and HBP (Fig. 6A). To characterize the metabolic features of PYGL-mediated glycogen phosphorylase in microglia under AD pathology and to further elucidate the molecular mechanisms by which PYGL regulates microglial autophagy, we next investigated the downstream metabolic pathways affected by PYGL in microglial glycogen catabolism. The ECAR serves as a key indicator of cellular glycolytic activity. Stimulation with Aβ enhanced both the basal and maximal glycolytic capacities of microglia, whereas PYGL knockdown resulted in only a slight reduction in basal glycolysis without significantly altering the maximal glycolytic capacity (Fig. 6B−D). These findings suggest that PYGL exerts a minimal regulatory effect on glycolytic metabolism in microglia. Subsequently, we assessed the metabolic activity of the PPP, for which NADPH/$NADP^+$ and GSH/GSSG are considered key indicators[15]. Following Aβ exposure, both NADPH/$NADP^+$ and GSH/GSSG levels were significantly elevated in primary microglia. Interestingly, PYGL knockdown further enhanced these levels (Fig. 6E and F), a finding that was somewhat unexpected. Next, we conducted untargeted metabolomic profiling to further investigate the characteristics of PYGL knockdown on glycogen catabolism in primary microglia. PCA revealed clear separation among the experimental groups, indicating high reproducibility within groups and reliable data quality (Fig. 6G). Volcano plots identified significant changes in metabolite abundance across groups: compared with the si-NC group, the si-NC + Aβ groups showed 33 upregulated and 19 downregulated metabolites; in addition, compared with the si-NC + Aβ group, the si-PYGL + Aβ group displayed 31 upregulated and 29 downregulated metabolites (Fig. 6H and I, Supporting Information Table S4). Notably, 17 differential metabolites were shared between the si-NC + Aβ *vs*. si-NC and si-NC + Aβ *vs*. si-PYGL + Aβ comparisons (Fig. 6J), as shown in the heatmap (Fig. 6K). Focusing on the PPP, the levels of X5P and R5P remained unchanged in the si-NC + Aβ group *vs*. si-NC, whereas the S7P and E4P levels were elevated. Upon PYGL knockdown, R5P showed increased abundance, but X5P, S7P, and E4P levels remained unaltered compared with the si-NC + Aβ group (Fig. 6L). Furthermore, our metabolic flux analysis results indicated that knocking down PYGL did not significantly alter the levels of the TCA metabolites m+2 labeled citrate and m+2 labeled succinate (Supporting Information Fig. S9A and S9B), nor did it significantly change the levels of the PPP metabolites m+4 labeled E4P and m+7 labeled S7P in microglia under Aβ stimulation (Fig. S9C and S9D). These findings suggest that the knockdown of PYGL does not directly affect the PPP pathway in microglia. We observed that the HBP metabolite UDP-GlcNAc was significantly elevated in primary microglia following Aβ treatment, but this increase was markedly reversed by PYGL knockdown. Notably, UDP-GlcNAc was the most significantly downregulated metabolite upon PYGL knockdown in Aβ treated primary microglia (Fig. 6I).

The primary products of glycogenolysis are G6P and glucosamine[41]. We extracted and purified the glycogen granules of Aβ-treated microglia and found that the level of glucosamine in glycogen was significantly increased after PYGL knockdown (Fig. 6M). Importantly, knocking down PYGL reduced the levels of free glucosamine (Fig. 6N) and free UDP-GlcNAc (Fig. 6O) in microglia following Aβ stimulation, while it increased free G6P levels (Fig. 6P). Moreover, the metabolic flux analysis results indicated that knocking down PYGL significantly reduced the level of m+13 labeled UDP-GlcNAc (Fig. 6Q). These results confirm that in microglia, the carbon source derived from PYGL-mediated glycogenolysis primarily supports the HBP.

Further functional enrichment analysis of the differential metabolites revealed that many were linked to pathways involved in post-translational protein modification and glycosylation precursor biosynthesis (Fig. S9E), which was also reflected in the metabolite-pathway interaction network (Fig. S9F). Based on these observations, we hypothesized that PYGL-dependent glycogen catabolism may regulate microglial autophagy through modulation of *O*-GlcNAcylation. Consistent with this hypothesis, *O*-GlcNAcylation assays demonstrated that Aβ treatment markedly elevated primary microglial total cellular *O*-GlcNAcylation. Both PYGL knockdown and pharmacological inhibition of PYGL with glycogen phosphorylase inhibitor reversed this trend (Fig. 6R

efficiency of primary microglia assessed by flow cytometry following HiLyte-Aβ_{42} uptake ($n=$ 3 independent experiments). (O, P) Colocalization of HiLyte-Aβ_{42} with lysosomes in primary microglia assessed by immunofluorescence ($n=$ 3−4 per sample with $n=$ 3 samples/group, total $n=$ 10). (Q, R) Immunofluorescence was used to detect the number of HiLyte-Aβ_{42} per microglial cell ($n=$ 10 per sample with $n=$ 4 samples/group, total $n=$ 40). Quantitative data are presented as the mean ± SD; *$P<$ 0.05; **$P<$ 0.01; ***$P<$ 0.001; ****$P<$ 0.0001.

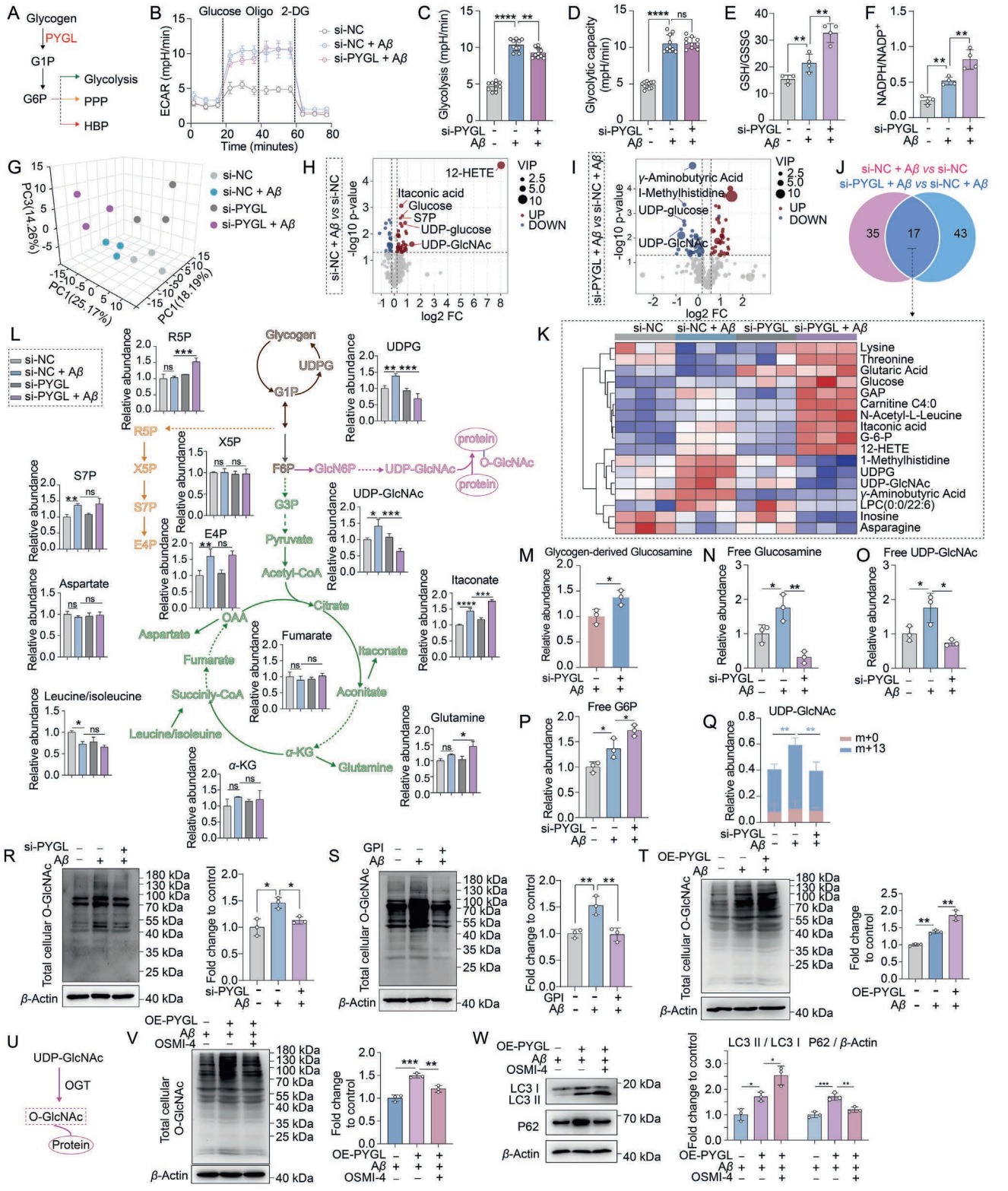

Figure 6 Knockdown of microglial PYGL suppresses HBP metabolism to reduce O-glycosylation levels. (A) Schematic of glycogen metabolic pathways. (B) Seahorse analysis of ECAR in primary microglia ($n=$ 10 donors per group). (C, D) Seahorse analysis of glycolysis and glycolytic capacity in primary microglia ($n=$ 10 donors per group). (E) GSH/GSSG in primary microglia ($n=$ 4 independent experiments). (F) NADPH/NADP+ in primary microglia ($n=$ 4 independent experiments). (G) PCA of primary microglial metabolomes following untargeted metabolomics ($n=$ 3 cell samples). (H, I) Differential metabolites identified in si-NC + Aβ *vs*. si-NC (H) and si-PYGL + Aβ *vs*. si-NC + Aβ (I). (J, K) Shared differential metabolites among three comparison groups (J), and their abundance across groups (K). (L) Relative abundance of differentially expressed metabolites in primary microglia. (M) Relative abundance of glycogen-derived glucosamine in primary microglia ($n=$ 3 independent

and S). Moreover, the addition of OGA nearly abolished all *O*-GlcNAc signals (Supporting Information Fig. S10A), which confirmed the specificity of the *O*-GlcNAc signals detected in this study. By contrast, PYGL overexpression further enhanced Aβ-induced total cellular *O*-GlcNAcylation in microglia (Fig. 6T). *O*-GlcNAc transferase (OGT) is the key enzyme responsible for the addition of *O*-GlcNAc to target proteins (Fig. 6U). Pharmacological inhibition of OGT with OSMI-4[53] abrogated the increase in *O*-GlcNAcylation induced by PYGL overexpression and restored autophagic flux in primary microglia (Fig. 6V and W). Although our data also showed that knocking down PYGL significantly reduced UDPG levels (Fig. 6I and K), we did not observe any effect of exogenous UDPG supplementation on the LC3 II/I ratio or P62 expression in Aβ-treated microglia (Supporting Information Fig. S11A−S11C). This suggests that PYGL-mediated glycogen catabolism does not regulate autophagy levels through UDPG. Collectively, these findings establish that PYGL-mediated glycogen catabolism primarily modulates HBP, thereby affecting *O*-GlcNAcylation and regulating microglial autophagy.

3.6. PYGL regulates autophagosome−lysosome fusion by modulating the O-GlcNAcylation of SNAP29

The soluble *N*-ethylmaleimide-sensitive factor attachment protein receptor (SNARE) complex, composed of SNAP29, STX17, and VAMP8, plays a pivotal role in regulating autophagosome−lysosome fusion, and its assembly is critically modulated by the *O*-GlcNAcylation of SNAP29[42] (Fig. 7A). Based on these findings, we hypothesized that in the context of AD, PYGL may impair SNARE complex assembly by promoting *O*-GlcNAcylation of SNAP29, consequently disrupting autophagosome−lysosome fusion and ultimately arresting microglial autophagic flux. Therefore, we first observed the level of *O*-GlcNAcylation of SNAP29 after PYGL knockdown. As shown in Fig. 7B and C, HA-SNAP29 plasmids were transfected to overexpress SNAP29 in microglia, and Aβ stimulation enhanced the *O*-GlcNAcylation of SNAP29, whereas PYGL knockdown significantly reversed this effect, as detected by Co-IP. The addition of OGA nearly abolished all *O*-GlcNAc signals (Supporting Information Fig. S12A), which confirmed the specificity of the *O*-GlcNAc signals detected. Next, we examined the effect of PYGL modulation on SNARE complex assembly. Microglia were co-transfected with Flag-STX17, HA-SNAP29, and Myc-VAMP8 plasmids to overexpress these proteins. Co-IP assays using anti-Flag, anti-HA, and anti-Myc antibodies revealed that Aβ treatment disrupted the interactions among STX17, SNAP29, and VAMP8. Importantly, PYGL knockdown significantly restored these protein interactions (Fig. 7D−I). These results indicate that inhibiting PYGL-mediated glycogenolysis reduces SNAP29 *O*-GlcNAcylation and stabilizes SNARE complex assembly. Subsequently, we explored the role of SNAP29 *O*-GlcNAcylation in the Aβ-induced blockade of autophagic flux in microglia. We generated SNAP29 mutants (HA-SNAP29-QM) with *O*-GlcNAcylation sites mutated at S2A, S61G, T130A, and S153G (Supporting Information Table S5), as reported previously[42]. Co-IP assays confirmed that HA-SNAP29-QM markedly reduced SNAP29 *O*-GlcNAcylation levels (Fig. 7J and K). Crucially, transfection with HA-SNAP29-WT led to further increases in LC3II/I and P62 protein levels, whereas HA-SNAP29-QM increased the LC3II/I ratio but decreased P62 expression (Fig. 7L−N). These results demonstrate that *O*-GlcNAcylation of SNAP29 is essential for Aβ-induced inhibition of autophagic flux in microglia. Finally, we assessed whether PYGL regulates microglial autophagy by modulating SNAP29 *O*-GlcNAcylation. To this end, we knocked out endogenous SNAP29 in microglia *via* CRISPR-Cas9 (Supporting Information Fig. S13A), before transfecting with HA-SNAP29-WT or HA-SNAP29-QM. Western blotting analysis showed that PYGL overexpression increased the LC3II/I and P62 levels in microglia transfected with HA-SNAP29-WT but decreased P62 expression in microglia transfected with HA-SNAP29-QM (Fig. 7O−Q). These findings suggest that the regulation of microglial autophagy by PYGL-mediated glycogen catabolism is dependent on the *O*-GlcNAcylation of SNAP29.

4. Discussion

Emerging studies indicate that microglia in the AD brain undergo significant metabolic reprogramming, which critically influences their immune function and contributes to disease progression. While alterations in glucose and lipid metabolism have been extensively documented, the role of glycogen metabolism—particularly its catabolic branch—in microglial dysfunction during AD remains poorly understood. Our study identifies PYGL-mediated glycogenolysis as a key dysregulated pathway in AD-associated microglia and elucidates its mechanistic contribution to impaired autophagy and aggravated pathology.

A striking feature of microglia in AD is glycogen accumulation and the concurrent upregulation of both glycogen synthetic and catabolic enzymes, suggesting a state of dysregulated cycling rather than coherent metabolic adaptation. Our findings, together with a recent study[37], indicate that glycogen accumulation in microglia progresses with AD and correlates spatially with pathology both in AD patients and transgenic mice, as shown by the preferential localization of glycogen-laden microglia around Aβ plaques and dystrophic neurites. Regarding the mechanism underlying persistent glycogen accumulation, our omics data indicate that while glycophagy may be activated, the continued buildup of glycogen granules likely results from either excessive synthesis due to dysregulated glucose metabolism or inefficient clearance despite glycophagy activation. Within this dysregulated landscape, PYGL expression in microglia exhibits spatiotemporal specificity, correlating with Aβ plaque proximity and disease progression in AD patients, and in APP/PS1-21 and 5xFAD

experiments). (N−P) Relative abundance of free glucosamine, UDP-GlcNAc, and G6P in primary microglia ($n=$ 3 independent experiments). (Q) Isotopic tracing of $^{13}C_6$-glucose was employed to detect m+13-labeled UDP-GlcNAc ($n=$ 4 independent experiments). (R−T) Protein levels of total cellular *O*-GlcNAc in primary microglia treated with si-PYGL (R), Glycogen phosphorylase inhibitor (S), or OE-PYGL (T) in combination with Aβ ($n=$ 3 independent experiments). (U) Schematic diagram of the *O*-GlcNAcylation pathway. (V) Protein levels of total cellular *O*-GlcNAc in microglia treated with OE-PYGL, OSMI, and Aβ ($n=$ 3 independent experiments). (W) Protein levels of LC3II/I and P62 in microglia treated with OE-PYGL, OSMI, and Aβ ($n=$ 3 independent experiments). Quantitative data are presented as the mean ± SD; *$P<$ 0.05; **$P<$ 0.01; ***$P<$ 0.001; ****$P<$ 0.0001.

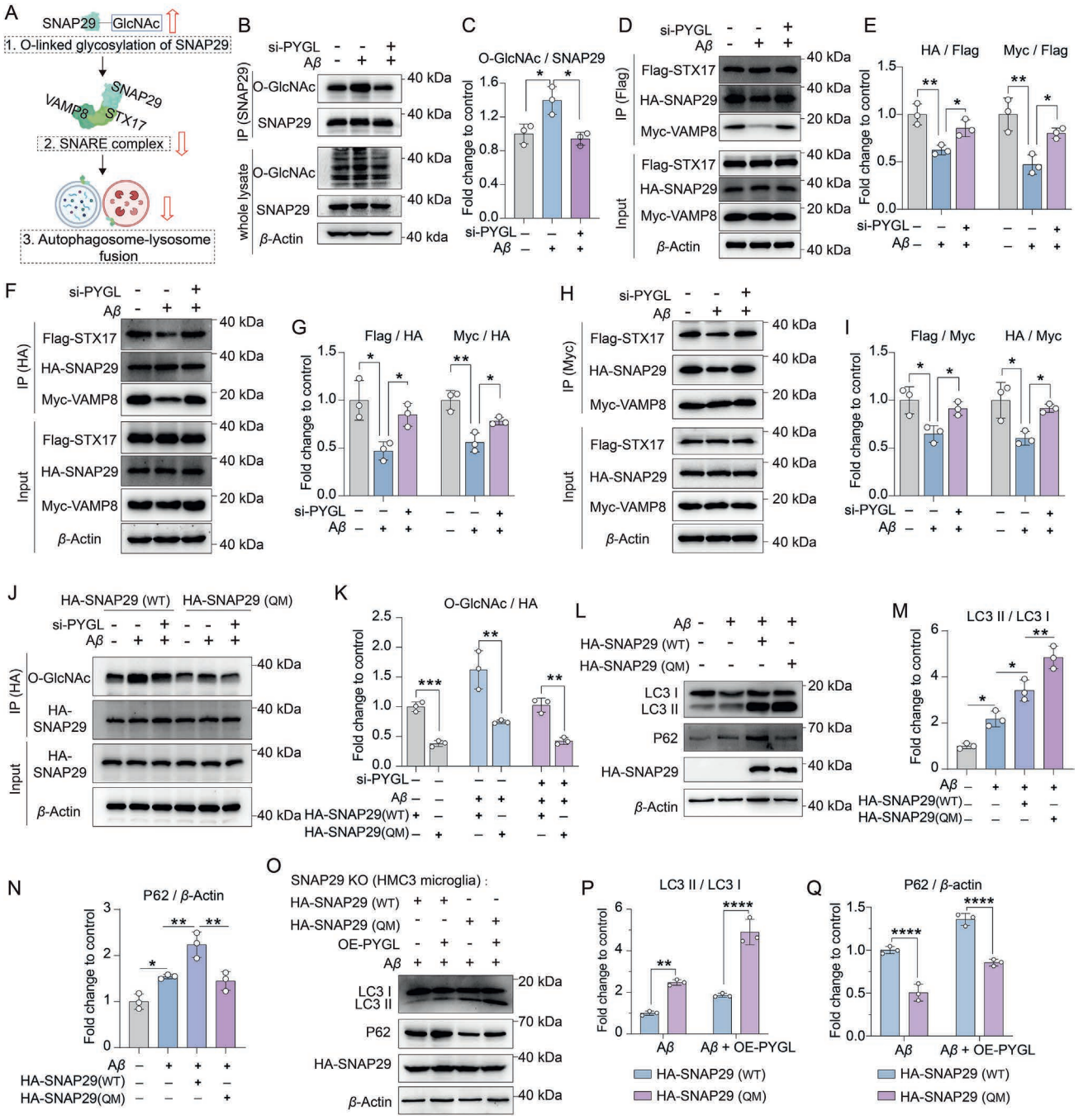

Figure 7 PYGL regulates autophagosome−lysosome fusion by modulating the *O*-GlcNAcylation of SNAP29. (A) Schematic of SNARE complex-mediated autophagosome−lysosome fusion. (B) Co-IP analysis of SNAP29 *O*-GlcNAcylation in HMC3 microglial cells. (C) Quantitative data shown in (B) ($n=$ 3 independent experiments). (D) Co-IP of Flag-STX17 to assess interactions with SNAP29 and VAMP8 in HMC3 microglial cells. (E) Quantitative data shown in (D) ($n=$ 3 independent experiments). (F) Co-IP of HA-SNAP29 to assess interactions with STX17 and VAMP8 in HMC3 microglial cells. (G) Quantitative data shown in (F) ($n=$ 3 independent experiments). (H) Co-IP of Myc-VAMP8 to assess interactions with SNAP29 and STX17 in HMC3 microglial cells. (I) Quantitative data shown in (H) ($n=$ 3 independent experiments). (J) *O*-GlcNAcylation levels of SNAP29 after transfection with HA-SNAP29 (WT) and HA-SNAP29 (QM) were assessed by Co-IP in HMC3 microglial cells. (K) Quantitative data shown in (J) ($n=$ 3 independent experiments). (L) Protein levels of LC3II/I and P62 after transfection with HA-SNAP29 (WT) and HA-SNAP29 (QM) in HMC3 microglial cells. (M, N) Quantitative data shown in (L) ($n=$ 3 independent experiments). (O) Protein levels of LC3II/I and P62 after transfection with HA-SNAP29 (WT) and HA-SNAP29 (QM) in HMC3 microglial cells with SNAP29 CRISPR knockout. (P, Q) Quantitative data shown in (O) ($n=$ 3 independent experiments). Quantitative data are presented as the mean ± SD; $^{*}P<0.05$; $^{**}P<0.01$; $^{***}P<0.001$; $^{****}P<0.0001$.

(Supporting Information Fig. S14A and S14B) transgenic mice. Functionally, microglia-specific PYGL knockdown ameliorated key AD pathologies—neuroinflammation, amyloid burden, and memory deficits—in APP/PS1-21 and in 5xFAD (Fig. S14C−S14G) transgenic mice. This establishes microglial glycogenolysis firmly within the pathogenic cascade of AD, and helps reconcile conflicting literature on the role of brain glycogen in cognition. While prior studies reporting beneficial effects of glycogen turnover typically focused on physiological memory formation in young organisms[54,55], our data, together with other related evidence[19] indicate that in the aged, neurodegenerative brain, sustained microglial glycogenolysis becomes detrimental, underscoring a critical context-dependency in brain energy metabolism.

A central question arising from our findings is how elevated glycogenolysis impairs microglial function. Our multi-omics and functional analyses identified autophagy as the primary process affected. PYGL knockdown enhanced autophagic flux, specifically promoting autophagosome−lysosome fusion, in both Aβ42-treated microglia and microglia isolated from APP/PS1-21 and 5xFAD (Fig. S14H−S14J) transgenic mice. Mounting evidence establishes autophagic dysfunction as an important pathogenic driver in AD[56], with microglial autophagy playing a pivotal role in Aβ clearance and neuroinflammatory control[57-59]. Although autophagy can be activated in plaque-associated microglia, its suppression exacerbates pathology, highlighting the importance of functional flux over mere induction[50,51,60,61]. Therefore, the restoration of autophagic activity following PYGL knockdown provides a direct mechanistic link between aberrant glycogen metabolism and the compromised cellular clearance pathways central to AD progression.

Our findings uncovered a pathogenic rewiring of glycogen catabolism in AD microglia, wherein PYGL-mediated glycogenolysis preferentially fuels the HBP in microglia. This diversion of carbon flux leads to increased UDP-GlcNAc levels and a consequent rise in global protein *O*-GlcNAcylation, directly linking glycogen breakdown to a widespread post-translational modification program. Our data reveal a critical functional shift: in Aβ-stimulated microglia, glycogenolysis serves not primarily to meet bioenergetic demands, but to supply substrates for protein glycosylation. This mechanism represents a distinct, pathology-dependent stratification of immunometabolism. In other immune contexts, such as in activated dendritic cells or $CD8^+$ memory T cells, glycogen breakdown is rapidly deployed to support energy production or redox balance through the PPP[21,22]. Although the levels of some metabolites, such as R5P and Itcotate, were increased after PYGL knockdown. Integrating metabolic flux and metabolomic data, we propose that under Aβ stimulation, carbon from PYGL-mediated glycogenolysis is not primarily channeled into the TCA cycle or the PPP, and the changes observed in some TCA and PPP metabolites likely reflect adaptive metabolic fluctuations secondary to the improved immune and autophagic function of microglia after PYGL knockdown—such as adjustments in energy demand and redox balance. In other words, glycogenolysis likely regulates the PPP and the TCA indirectly—modulating its function—rather than acting as a major direct supplier of carbon skeletons.

We identified SNAP29, a core SNARE protein required for autophagosome−lysosome fusion, as the critical target linking *O*-GlcNAcylation to autophagy impairment. The SNARE complex, a protein assembly complex responsible for regulating autophagosome−lysosome fusion, plays a critical role in sustaining autophagic flux[62,63]. SNAP29 is one of the core components of the SNARE complex, and the *O*-GlcNAcylation level of SNAP29 determines autophagosome maturation in mammalian cells[64,65]. PYGL-driven glycosylation of SNAP29 impaired its assembly into functional SNARE complexes, thereby stalling autophagosome maturation. Crucially, mutating the *O*-GlcNAc sites on SNAP29 not only restored autophagic flux but also fully reversed the inhibitory effect of PYGL overexpression. In AD, SNAP29-mediated autophagy correlates with IL-1β release and neuroinflammation[66], while SNARE complex stability contributes to intracellular Aβ clearance in neurons[67]. These establish SNAP29 *O*-GlcNAcylation as the precise molecular mechanism through which aberrant glycogenolysis disrupts autophagic flux of microglia in AD, directly connecting metabolic dysregulation to impaired proteostasis.

Several important limitations and future directions emerge from this work. First, other peripheral immune cells and central nervous system cells also express other PYG isoforms[21,22], which may similarly be involved in AD pathological progression. The translational potential of targeting microglial PYGL requires careful evaluation. Second, the global *O*-GlcNAcylome in AD microglia remains largely unmapped; systematic profiling could reveal additional modified proteins that influence inflammation, phagocytosis, or cell survival. Third, future studies using inducible knockouts or small-molecule inhibitors in advanced disease stages will be crucial for assessing therapeutic windows.

5. Conclusions

Our work elucidates the characteristics of aberrant PYGL-mediated glycogenolysis in microglia under AD pathological conditions and reveals its key mechanistic role in regulating *O*-GlcNAcylation and enhancing autophagic flux. Thus, targeting PYGL-mediated glycogenolysis may serve as an immunometabolic therapeutic strategy for AD by enhancing microglial autophagic function.

Acknowledgments

This work was supported by the National Natural Science Foundation of China (82401689, 82471218), Postdoctoral Fellowship Program of CPSF (GZC20231153, China), Science Innovation 2030-Brain Science and Brain-Inspired Intelligence Technology Major Project (#2021ZD0201100 Task 4 #2021ZD0201104) and Postgraduate Research and Practice Innovation Program of Jiangsu Province (No. JX10114228, China). We thank Fan Hu (Nanjing Medical University) for supporting our imaging experiments and analysis using confocal microscopy. And we also thank LetPub (www.letpub.com.cn) for its linguistic assistance during the preparation of this manuscript.

Author contributions

Lei Li, Zhi-Yuan Zhang, and Yong-Jie Zhang conceived this project. Yi Ding, Shi-Yao Li, and Wen-Feng Zhang performed most experiments and analyzed the data. Mao-Mao Chu, Xue-Jie Wang, Yu-Ge Zhang, and Hui-Wen Zhang performed AAVs injection and behavioral tests. Yi Ding, Yu-Tong Zhang, and Lu Xu performed the RNA sequencing experiments and bioinformatics analysis. Xue Liu and Zi-Jian Ren assisted in data collection and visualization. Tsuyoshi Morita and Otto Baba contributed to methodology. Lei Li, Zhi-Yuan Zhang, and Yi Ding wrote the

manuscript with input from all authors. Lei Li and Zhi-Yuan Zhang supervised the project and revised the manuscript. Lei Li, Zhi-Yuan Zhang, Hui-Wen Zhang, and Yong-Jie Zhang acquired funds.

Conflicts of interest

The authors declare no conflicts of interest.

Appendix A. Supporting information

Supporting information to this article can be found online at https://doi.org/10.1016/j.apsb.2026.04.017.

References

1. Austad SN, Ballinger S, Buford TW, Carter CS, Smith Jr DL, Darley-Usmar V, et al. Targeting whole body metabolism and mitochondrial bioenergetics in the drug development for Alzheimer's disease. *Acta Pharm Sin B* 2022;**12**:511−31.
2. Karran E, De Strooper B. The amyloid hypothesis in Alzheimer disease: new insights from new therapeutics. *Nat Rev Drug Discov* 2022; **21**:306−18.
3. Jung ES, Choi H, Mook-Jung I. Decoding microglial immunometabolism: a new frontier in Alzheimer's disease research. *Mol Neurodegener* 2025;**20**:37.
4. Ottoy J, Niemantsverdriet E, Verhaeghe J, De Roeck E, Struyfs H, Somers C, et al. Association of short-term cognitive decline and MCI-to-AD dementia conversion with CSF, MRI, amyloid- and ^{18}F-FDG-PET imaging. *Neuroimage Clin* 2019;**22**:101771.
5. Efthymiou AG, Goate AM. Late onset Alzheimer's disease genetics implicates microglial pathways in disease risk. *Mol Neurodegener* 2017;**12**:43.
6. Sudwarts A, Thinakaran G. Alzheimer's genes in microglia: a risk worth investigating. *Mol Neurodegener* 2023;**18**:90.
7. Shemer A, Erny D, Jung S, Prinz M. Microglia plasticity during health and disease: an immunological perspective. *Trends Immunol* 2015;**36**: 614−24.
8. Bernier LP, York EM, Kamyabi A, Choi HB, Weilinger NL, MacVicar BA. Microglial metabolic flexibility supports immune surveillance of the brain parenchyma. *Nat Commun* 2020;**11**:1559.
9. Yang S, Qin C, Hu ZW, Zhou LQ, Yu HH, Chen M, et al. Microglia reprogram metabolic profiles for phenotype and function changes in central nervous system. *Neurobiol Dis* 2021;**152**:105290.
10. Li L, Cheng SQ, Sun YQ, Yu JB, Huang XX, Dong YF, et al. Resolvin D1 reprograms energy metabolism to promote microglia to phagocytize neutrophils after ischemic stroke. *Cell Rep* 2023;**42**:112617.
11. Ulland TK, Song WM, Huang SC, Ulrich JD, Sergushichev A, Beatty WL, et al. TREM2 maintains microglial metabolic fitness in Alzheimer's disease. *Cell* 2017;**170**. 649-63.e13.
12. Friday CM, Stephens IO, Smith CT, Lee S, Satish D, Devanney NA, et al. APOE4 reshapes the lipid droplet proteome and modulates microglial inflammatory responses. *Neurobiol Dis* 2025;**212**:106983.
13. Haney MS, Palovics R, Munson CN, Long C, Johansson PK, Yip O, et al. APOE4/4 is linked to damaging lipid droplets in Alzheimer's disease microglia. *Nature* 2024;**628**:154−61.
14. Victor MB, Leary N, Luna X, Meharena HS, Scannail AN, Bozzelli PL, et al. Lipid accumulation induced by APOE4 impairs microglial surveillance of neuronal-network activity. *Cell Stem Cell* 2022;**29**. 1197-212.e8.
15. Pan RY, He L, Zhang J, Liu X, Liao Y, Gao J, et al. Positive feedback regulation of microglial glucose metabolism by histone H4 lysine 12 lactylation in Alzheimer's disease. *Cell Metab* 2022;**34**. 634-48.e6.
16. Leng L, Yuan Z, Pan R, Su X, Wang H, Xue J, et al. Microglial hexokinase 2 deficiency increases ATP generation through lipid metabolism leading to beta-amyloid clearance. *Nat Metab* 2022;**4**: 1287−305.
17. Liu X, Gilbert RG. Normal and abnormal glycogen structure—a review. *Carbohydr Polym* 2024;**338**:122195.
18. Ma J, Wei K, Liu J, Tang K, Zhang H, Zhu L, et al. Glycogen metabolism regulates macrophage-mediated acute inflammatory responses. *Nat Commun* 2020;**11**:1769.
19. Minhas PS, Latif-Hernandez A, McReynolds MR, Durairaj AS, Wang Q, Rubin A, et al. Restoring metabolism of myeloid cells reverses cognitive decline in ageing. *Nature* 2021;**590**:122−8.
20. Drulis-Fajdasz D, Krzystyniak A, Puscian A, Pytys A, Gostomska-Pampuch K, Pudelko-Malik N, et al. Glycogen phosphorylase inhibition improves cognitive function of aged mice. *Aging Cell* 2023;**22**: e13928.
21. Thwe PM, Pelgrom LR, Cooper R, Beauchamp S, Reisz JA, D'Alessandro A, et al. Cell-intrinsic glycogen metabolism supports early glycolytic reprogramming required for dendritic cell immune responses. *Cell Metab* 2019;**30**:225.
22. Zhang H, Liu J, Yang Z, Zeng L, Wei K, Zhu L, et al. TCR activation directly stimulates PYGB-dependent glycogenolysis to fuel the early recall response in CD8$^+$ memory T cells. *Mol Cell* 2022;**82**. 3077-88.e6.
23. Han Z, Zhang W, Ning W, Wang C, Deng W, Li Z, et al. Model-based analysis uncovers mutations altering autophagy selectivity in human cancer. *Nat Commun* 2021;**12**:3258.
24. Oe Y, Baba O, Ashida H, Nakamura KC, Hirase H. Glycogen distribution in the microwave-fixed mouse brain reveals heterogeneous astrocytic patterns. *Glia* 2016;**64**:1532−45.
25. Huang L, Jin J, Chen K, You S, Zhang H, Sideris A, et al. BDNF produced by cerebral microglia promotes cortical plasticity and pain hypersensitivity after peripheral nerve injury. *PLoS Biol* 2021;**19**: e3001337.
26. Chen S, Chang Y, Li L, Acosta D, Li Y, Guo Q, et al. Spatially resolved transcriptomics reveals genes associated with the vulnerability of middle temporal gyrus in Alzheimer's disease. *Acta Neuropathol Commun* 2022;**10**:188.
27. Solga AC, Pong WW, Kim KY, Cimino PJ, Toonen JA, Walker J, et al. RNA sequencing of tumor-associated microglia reveals Ccl5 as a stromal chemokine critical for neurofibromatosis-1 glioma growth. *Neoplasia* 2015;**17**:776−88.
28. Ding Y, Li SY, Lv W, Li L, Zhang HW, Zhang Z, et al. Pyroptosis signature gene CHMP4B regulates microglia pyroptosis by inhibiting GSDMD in Alzheimer's disease. *Mol Neurobiol* 2025;**62**:77−90.
29. Xu L, Li L, Pan CL, Song JJ, Zhang CY, Wu XH, et al. Erythropoietin signaling in peripheral macrophages is required for systemic beta-amyloid clearance. *EMBO J* 2022;**41**:e111038.
30. Chromy BA, Nowak RJ, Lambert MP, Viola KL, Chang L, Velasco PT, et al. Self-assembly of Abeta$_{1-42}$ into globular neurotoxins. *Biochemistry* 2003;**42**:12749−60.
31. Dahlgren KN, Manelli AM, Stine Jr WB, Baker LK, Krafft GA, LaDu MJ. Oligomeric and fibrillar species of amyloid-beta peptides differentially affect neuronal viability. *J Biol Chem* 2002;**277**: 32046−53.
32. Stine WB Jr, Dahlgren KN, Krafft GA, LaDu MJ. *In vitro* characterization of conditions for amyloid-beta peptide oligomerization and fibrillogenesis. *J Biol Chem* 2003;**278**:11612−22.
33. Nazer B, Hong S, Selkoe DJ. LRP promotes endocytosis and degradation, but not transcytosis, of the amyloid-beta peptide in a blood−brain barrier *in vitro* model. *Neurobiol Dis* 2008;**30**:94−102.
34. Vestergaard M, Hamada T, Saito M, Yajima Y, Kudou M, Tamiya E, et al. Detection of Alzheimer's amyloid beta aggregation by capturing molecular trails of individual assemblies. *Biochem Biophys Res Commun* 2008;**377**:725−8.
35. Gaida D, Park YW, Kang YJ, Kim SG. Therapeutic potential of 4-hexylresorcinol in reducing sarcopenia in diabetic masseter muscle. *Maxillofac Plast Reconstr Surg* 2025;**47**:2.
36. Xu M, Zhou F, Ahmed O, Randle LV, Shin JK, Zhu Y, et al. Dual lactate clearance in the viability assessment of livers donated after

circulatory death with *ex situ* normothermic machine perfusion. *Transplant Direct* 2021;**7**:e789.
37. St-Pierre MK, Carrier M, Gonzalez Ibanez F, Simoncicova E, Wallman MJ, Vallieres L, et al. Ultrastructural characterization of dark microglia during aging in a mouse model of Alzheimer's disease pathology and in human post-mortem brain samples. *J Neuroinflammation* 2022;**19**:235.
38. Johannesson M, Soderberg L, Zachrisson O, Fritz N, Kylefjord H, Gkanatsiou E, et al. Lecanemab demonstrates highly selective binding to Abeta protofibrils isolated from Alzheimer's disease brains. *Mol Cell Neurosci* 2024;**130**:103949.
39. Zhang J, Wang Y, Dong X, Liu J. Crocetin attenuates inflammation and amyloid-beta accumulation in APPsw transgenic mice. *Immun Ageing* 2018;**15**:24.
40. Parkinson J, Ploeger B, Appelkvist P, Bogstedt A, Dillner Bergstedt K, Eketjall S, et al. Modeling of age-dependent amyloid accumulation and gamma-secretase inhibition of soluble and insoluble Abeta in a transgenic mouse model of amyloid deposition. *Pharmacol Res Perspect* 2013;**1**:e00012.
41. Sun RC, Young LEA, Bruntz RC, Markussen KH, Zhou Z, Conroy LR, et al. Brain glycogen serves as a critical glucosamine cache required for protein glycosylation. *Cell Metab* 2021;**33**. 1404-17.e9.
42. Guo B, Liang Q, Li L, Hu Z, Wu F, Zhang P, et al. *O*-GlcNAc-modification of SNAP-29 regulates autophagosome maturation. *Nat Cell Biol* 2014;**16**:1215−26.
43. Minhas PS, Jones JR, Latif-Hernandez A, Sugiura Y, Durairaj AS, Wang Q, et al. Restoring hippocampal glucose metabolism rescues cognition across Alzheimer's disease pathologies. *Science* 2024;**385**. eabm6131.
44. Chen T, Pan F, Huang Q, Xie G, Chao X, Wu L, et al. Metabolic phenotyping reveals an emerging role of ammonia abnormality in Alzheimer's disease. *Nat Commun* 2024;**15**:3796.
45. Haythorne E, Rohm M, van de Bunt M, Brereton MF, Tarasov AI, Blacker TS, et al. Diabetes causes marked inhibition of mitochondrial metabolism in pancreatic beta-cells. *Nat Commun* 2019;**10**:2474.
46. Prats C, Graham TE, Shearer J. The dynamic life of the glycogen granule. *J Biol Chem* 2018;**293**:7089−98.
47. Parhizkar S, Gent G, Chen Y, Rensing N, Gratuze M, Strout G, et al. Sleep deprivation exacerbates microglial reactivity and Abeta deposition in a TREM2-dependent manner in mice. *Sci Transl Med* 2023;**15**. eade6285.
48. Krasemann S, Madore C, Cialic R, Baufeld C, Calcagno N, El Fatimy R, et al. The TREM2−APOE pathway drives the transcriptional phenotype of dysfunctional microglia in neurodegenerative diseases. *Immunity* 2017;**47**. 566-81.e9.
49. Wang H, Ye J, Peng Y, Ma W, Chen H, Sun H, et al. CKLF induces microglial activation *via* triggering defective mitophagy and mitochondrial dysfunction. *Autophagy* 2024;**20**:590−613.
50. Choi I, Wang M, Yoo S, Xu P, Seegobin SP, Li X, et al. Autophagy enables microglia to engage amyloid plaques and prevents microglial senescence. *Nat Cell Biol* 2023;**25**:963−74.
51. Cho MH, Cho K, Kang HJ, Jeon EY, Kim HS, Kwon HJ, et al. Autophagy in microglia degrades extracellular beta-amyloid fibrils and regulates the NLRP3 inflammasome. *Autophagy* 2014;**10**:1761−75.
52. Pomilio C, Gorojod RM, Riudavets M, Vinuesa A, Presa J, Gregosa A, et al. Microglial autophagy is impaired by prolonged exposure to beta-amyloid peptides: evidence from experimental models and Alzheimer's disease patients. *GeroScience* 2020;**42**:613−32.
53. Yao H, Liang C, Wang X, Duan C, Song X, Shang Y, et al. OGT-mediated *O*-GlcNAcylation of ATF2 protects against sepsis-associated encephalopathy by inhibiting microglial pyroptosis. *Neurosci Bull* 2025;**41**:1761−78.
54. Sinadinos C, Valles-Ortega J, Boulan L, Solsona E, Tevy MF, Marquez M, et al. Neuronal glycogen synthesis contributes to physiological aging. *Aging Cell* 2014;**13**:935−45.
55. Duran J, Saez I, Gruart A, Guinovart JJ, Delgado-Garcia JM. Impairment in long-term memory formation and learning-dependent synaptic plasticity in mice lacking glycogen synthase in the brain. *J Cereb Blood Flow Metab* 2013;**33**:550−6.
56. Li Y, Yang P, Meng R, Xu S, Zhou L, Qian K, et al. Multidimensional autophagy nano-regulator boosts Alzheimer's disease treatment by improving both extra/intraneuronal homeostasis. *Acta Pharm Sin B* 2024;**14**:1380−99.
57. Hellen M, Weert I, Muller SA, Rasanen N, Kettunen P, Lehtonen S, et al. Inflammation-induced lysosomal dysfunction in human iPSC-derived microglia is exacerbated by APOE 4/4 genotype. *J Neuroinflammation* 2025;**22**:147.
58. Mao M, Ma X, Wang X, Ye J. Microglial APOE4 promotes neuron degeneration in Alzheimer's disease through inhibition of lipid droplet autophagy. *Acta Pharm Sin B* 2025;**15**:657−60.
59. Cai Z, Wang S, Cao S, Chen Y, Penati S, Peng V, et al. Loss of ATG7 in microglia impairs UPR, triggers ferroptosis, and weakens amyloid pathology control. *J Exp Med* 2025;**222**:e20230173.
60. Heckmann BL, Teubner BJW, Tummers B, Boada-Romero E, Harris L, Yang M, et al. LC3-associated endocytosis facilitates beta-amyloid clearance and mitigates neurodegeneration in murine Alzheimer's disease. *Cell* 2019;**178**. 536-51.e14.
61. Berglund R, Guerreiro-Cacais AO, Adzemovic MZ, Zeitelhofer M, Lund H, Ewing E, et al. Microglial autophagy-associated phagocytosis is essential for recovery from neuroinflammation. *Sci Immunol* 2020;**5**. eabb5077.
62. Mukherjee R, Bhattacharya A, Tomaskovic I, Mello-Vieira J, Brunstein ME, Basoglu M, et al. Phosphoribosyl ubiquitination of SNARE proteins regulates autophagy during *Legionella* infection. *EMBO J* 2025;**44**:4252−79.
63. Cai R, Bai P, Quan M, Ding Y, Wei W, Liu C, et al. Migfilin promotes autophagic flux through direct interaction with SNAP29 and Vamp8. *J Cell Biol* 2024;**223**:e202312119.
64. Dodson M, Liu P, Jiang T, Ambrose AJ, Luo G, Rojo de la Vega M, et al. Increased *O*-GlcNAcylation of SNAP29 drives arsenic-induced autophagic dysfunction. *Mol Cell Biol* 2018;**38**. e00595-17.
65. Pellegrini FR, De Martino S, Fianco G, Ventura I, Valente D, Fiore M, et al. Blockage of autophagosome−lysosome fusion through SNAP29 *O*-GlcNAcylation promotes apoptosis *via* ROS production. *Autophagy* 2023;**19**:2078−93.
66. Hartmann J, Bajaj T, Otten J, Klengel C, Ebert T, Gellner AK, et al. SKA2 regulated hyperactive secretory autophagy drives neuroinflammation-induced neurodegeneration. *Nat Commun* 2024;**15**:2635.
67. Zhou X, Du K, Mao T, Wang N, Zhang L, Tian Y, et al. BMAL1 upregulates STX17 levels to promote autophagosome−lysosome fusion in hippocampal neurons to ameliorate Alzheimer's disease. *iScience* 2024;**27**:111413.